TAMPEREEN TEKNILLINEN YLIOPISTO
TAMPERE UNIVERSITY OF TECHNOLOGY

Leena Vuori

Nanofabrication and Adsorption Studies of Organic Molecules on Metal and Metal Alloy Surfaces as Templates for Biofunctional Applications

Julkaisu 1267 • Publication 1267

Tampere 2014

Tampereen teknillinen yliopisto. Julkaisu 1267
Tampere University of Technology. Publication 1267

Leena Vuori

Nanofabrication and Adsorption Studies of Organic Molecules on Metal and Metal Alloy Surfaces as Templates for Biofunctional Applications

Thesis for the degree of Doctor of Science in Technology to be presented with due permission for public examination and criticism in Tietotalo Building, Auditorium TB104, at Tampere University of Technology, on the 21st of November 2014, at 12 noon.

Tampereen teknillinen yliopisto - Tampere University of Technology
Tampere 2014

Doctoral candidate: Leena Vuori, M. Sc.
Surface Science Laboratory
Optoelectronics Research Centre
Tampere University of Technology

Supervisor: Mika Valden, professor
Surface Science Laboratory
Optoelectronics Research Centre
Tampere University of Technology

Pre-examiners: Claire-Marie Pradier, professor
Laboratoire de reactivite de surface
Universite Pierre et Marie Curie, Paris, France

Nora Kulak, assistant professor
Institute of Chemistry and Biochemistry
Department of Biology, Chemistry, Pharmacy
Freie Universität Berlin, Germany

Opponent: Jukka Matinlinna, Docent (University of Turku, Biomaterials Science)
Associate professor
Dental Materials Science
Faculty of Dentistry
The University of Hong Kong, Hong Kong SAR, PR China

ISBN 978-952-15-3410-2 (printed)
ISBN 978-952-15-3423-2 (PDF)
ISSN 1459-2045

ABSTRACT

The nanofabrication of organic layers on metal and metal alloy surfaces was studied in this thesis by employing photoelectron spectroscopy (PES) as the main analysis method. The motivation for this research is to introduce new properties to metal and metal alloy surfaces via self-assembly driven adsorption processes of organic molecules.

Trimesic acid (TMA) and glycine adsorption on single crystal Cu(100) surface was investigated with PES and scanning tunnelling microscopy (STM). TMA on Cu(100) exhibits coverage dependent surface phases with drastic changes in the molecular orientation. The mobile TMA molecules at low coverage transform into Cu atom coordinated TMA networks and finally into carboxyl (COOH) functionalized, densely packed TMA monolayers. This is enabled due to three equivalent COOH groups symmetrically around a rigid benzene ring. Homo- and heterochiral surface phases of achiral glycine on Cu(100) were observed, and a new structural model for glycine bonding on Cu(100) based on STM and density functional theory calculations is presented. The coadsorption of aminopropyl trimethoxysilane (APS) and mercaptopropyl trimethoxysilane (MPS) on stainless steel was studied with an aim to incorporate MPS in APS matrix with tuneable distribution.

In addition to the determination of elemental and chemical states at the surface, PES data was also used to determine the surface morphology by employing inelastic electron energy-loss background analysis. Synchrotron radiation mediated PES enabled the study of the in-depth distribution of the chemical states in non-destructive manner. The functionality of the APS/MPS overlayers on stainless steel was studied with chemical derivatization.

The studies of TMA and glycine on Cu(100) provide important knowledge of the adsorption behaviour of small molecules on surfaces, which is crucial for understanding the adsorption phenomena of larger molecules, such as proteins on more complex substrates. The fabricated surface structures may also be applicable to molecular electronics or catalytic surfaces. The bifunctional silanization of stainless steel, on the other hand, is directly transferrable to industrial scale processes. The bifunctional APS/MPS nanomolecular layer on stainless steel works as a template, to which biomolecules can be covalently coupled with tuneable distribution. Hence, the stainless steel surface can be biofunctionalized for a range of applications, depending on the properties of the biomolecules.

ACKNOWLEDGEMENTS

I would like to express my gratitude to my supervisor, prof. Mika Valden, for giving me the opportunity to work in his group, for all the support and trust during this work and especially for giving me an opportunity to pursue a career in research after working elsewhere for a long time.

I want to thank my present and former colleagues at Surface Science Laboratory, Dr. Marko Ahonen, Dr. Harri Ali-Löytty, Dr. Leila Costelle, M. Sc. Markku Hannula, Dr. Mika Hirsimäki, M.Sc. Niina Jokinen, Dr. Petri Jussila, Dr. Mikhail Kuzmin, Dr. Kimmo Lahtonen, M.Sc. Elina Lehtonen, Mr Jesse Saari, Ms Emmi Turppa and all the rest past and present co-workers for an inspiring working environment, for all the support and help, as well as (sometimes weird) conversations about Life, Universe and Everything. I also wish to thank Eija Heliniemi, Taina Meriläinen and Anne Viherkoski for a lot of help in all work related issues.

The research of this thesis was done in collaboration with the Protein Dynamics group of Institute of Biomedical Technology, University of Tampere. I would like to thank Dr. Vesa Hytönen, Mr. Ville Hynninen, Dr. Jenni Leppiniemi and Dr. Jenita Pärssinen for conducting the biofunctionalization studies of silanes on stainless steel. A part of the research was conducted at the synchrotron radiation facility MAX IV Laboratory, and I wish to thank Alexei Preobrajenski, the beam line manager of D1011, for all the help, as well as professor Ergo Nõmmiste, Dr. Rainer Pärna and Arvo Tõnisoo from the University of Tartu for participating at the beam line. I also would like to also thank Zhi-Xin Hu and Wei Ji at Renmin University of China for conducting the DFT calculations in Paper II.

I gratefully acknowledge the funders of this thesis: the National Graduate School of Material Physics, the Finland Centennial Foundation Fund for the Association of Finnish Steel and Metal Products, the Finnish Academy of Science and Letters, Vilho, Yrjö and Kalle Väisälä Foundation and the Jenny and Antti Wihuri Foundation.

My family and friends have been supportive and helpful during these years. I thank them all, especially Mika Lintujärvi for proof-reading. I wish to express my gratitude to all the men and boys at home: Joel, Juho and Arttu and especially Vesa for all the love, support and patience. This thesis is dedicated to my Dad, Ahti Vuori (1948 – 2004), for giving me the initial inspiration for science and technology.

Tampere, October 2014

Leena Vuori

CONTENTS

LIST OF PUBLICATIONS

The thesis consists of the following publications:

I. **L. Kanninen**, N. Jokinen, H. Ali-Löytty. P. Jussila, K. Lahtonen, M. Hirsimäki, M.Valden, M. Kuzmin, R. Pärna, E. Nõmmiste, ”Adsorption structure and bonding of trimesic acid on Cu(100)”, *Surface Science*, vol. 605, no. 23–24, pp. (1968–1978), 2011.

II. M. Kuzmin, K. Lahtonen, **L. Vuori**, Z.-X. Hu, W. Ji, M. Hirsimäki, and M. Valden, “Investigation of the structural anisotropy in a self-assembling glycinate layer on Cu(100) by scanning tunneling microscopy and density functional theory calculations”, submitted to *The Journal of Chemical Physics*.

III. **L. Vuori**, M. Hannula, K. Lahtonen, P. Jussila, H. Ali-Löytty, M. Hirsimäki, R. Pärna, E. Nõmmiste, and M. Valden, “Controlling the synergetic effects in (3-aminopropyl) trimethoxysilane and (3-mercaptopropyl) trimethoxysilane coadsorption on stainless steel surfaces”, *Applied Surface Science*, vol. 317, pp. (856-866), 2014.

IV. **L. Vuori**, J. Leppiniemi, M. Hannula, K. Lahtonen, M. Hirsimäki, E. Nõmmiste, L. Costelle, V. P. Hytönen, and M. Valden, “Biofunctional hybrid materials: bimolecular organosilane monolayers on FeCr alloys”, *Nanotechnology*, vol. 25. no. 43. pp. 435603

[*] The surname of the author changed from Kanninen to Vuori in August 2012.

AUTHOR'S CONTRIBUTION TO THE PUBLICATIONS

The author planned and organized the experiments and was largely responsible for carrying out the sample preparation and PES experiments for papers I, III and IV. The author performed the major part of the PES analysis for papers I, III and IV and wrote the original manuscript for papers III and IV. The author performed the PES analysis in paper II and its supplementary material and contributed to the writing of the paper.

ABBREVIATIONS AND SYMBOLS

(ads)	Adsorbed
(aq)	Aqueous
(des)	Desorbed
(g)	Gas
(l)	Liquid
(s)	Solid
A	Adsorbate molecule
Å	Ångstrom (1 Å = 10^{-10} m = 0.1 nm)
A-A	Adsorbate-adsorbate interactions
APS	(3-Aminopropyl) trimethoxysilane, $NH_2(CH_2)_3Si(OCH)_3$
APTES	(3-Aminopropyl) triethoxysilane, $NH_2(CH_2)_3Si(OC_2H_5)_3$
A-S	Adsorbate-substrate interactions
ASTM	American Iron and Steel Institute
atm	Atmospheric conditions
C=O	Carbonyl
CAE	Constant analyser energy
COOH	Carboxyl
CRR	Constant retarding ratio
DFT	Density functional theory
DI	Deionized
DMSO	Dimethyl sulphoxide
EF-XPEEM	Energy filtered X-ray photoelectron emission microscopy
EN 1.4372	Fe-18Cr-6Mn-4Ni, ASTM-201
EN	European Standard (designation of steel grades)
ESCA	Electron spectroscopy for chemical analysis
EtOH	Ethanol
FAT	Fixed analyser transmission
fcc	face-centred cubic crystal structure
FRR	Fixed retarding ratio
FWHM	Full width half maximum
Gly	Glycine, 2-aminoacetic acid (NH_2COOH)
IEEB	Inelastic electron energy-loss background
IMFP	Inelastic mean free path of an electron
MAL-F	*N*-(4,4,5,5,6,6,7,7,8,8,9,9,9-Tridecafluorononyl)maleimide,
ML	Monolayer
MPS	(3-Mercaptopropyl) trimethoxysilane, $SH(CH_2)_3Si(OCH_3)_3$
NH_2	Amino
OC_2H_5	Ethoxy
OCH_3	Methoxy
OH	Hydroxyl
PEEM	Photoelectron emission microscopy
PEG	Polyethylene glycol
PES	Photoelectron spectroscopy
PVD	Physical vapour deposition
R	Organofunctional group
S	Substrate atom
SAM	Self-assembled monolayer

SH	Thiol
SIL1	APS 0.10/MPS 0.01
SIL2	APS 0.10/MPS 1.00
SS	Stainless steel
SS-EC	Electrochemically treated stainless steel
TCEP	Tris(carboxyethyl) phosphine hydrochlorine
TMA	Trimesic acid, 1,3,5 –benzene tricarboxylic acid, $(C_6H_3(COOH)_3)$
UHV	Ultra high vacuum
X	Hydrolyzable group
XPS	X-ray photoelectron spectroscopy

$A(T)$	Universal cross section
c	Relative surface concentration
D	Degree of deprotonation
d	Adlayer height
E_0	Initial kinetic energy
E_B	Binding energy
E_K	Kinetic energy
F	Flux density of electrons
$f(x)$	Concentration of atoms at depth z
G	Electron energy distribution function
$h\nu$	Photon energy
i	Current density (A cm^{-2})
I	Intensity
J	PES spectrum
K	Instrumental constant
$K(E,T)$	Inelastic electron scattering cross section
$L_{ij}(\gamma)$	Angular symmetry factor for orbital j of element i
$n_i(z)$	Concentration of element i at distance z from the surface
q_i	Charge of the atom i
r_{ij}	Distance of atoms i and j
S_x	Sensitivity factor of species x
T	Total energy loss
$T(KE)$	Analyser transmission function
t_{exp}	Exposure time
T_S	Sample temperature
z	Depth

θ	Emission angle of electrons,
λ	Inelastic mean free path, IMFP
Ω	Solid angle
ϕ_S	Spectrometer work function
γ	Fraction of the surface covered by TMA
θ_{TMA}	TMA coverage
σ	Photoionization cross section

1. INTRODUCTION

The surfaces of solid materials and their interaction with surrounding media are of great importance, because the solid material surfaces often have unique functional properties due to different material composition from the bulk. By modifying the surface properties, new functional properties can be introduced to the material. Traditionally, metal and metal oxide surfaces have been treated with thick, micro- to millimetre scale coatings e.g. to improve corrosion or scratch resistance and to introduce adhesive properties or simply to enhance the appearance of the surface. These methods are viable for a large scale industrial production. For applications such as molecular recognition, heterogeneous catalysts, optoelectronics and biotechnology products, functional properties at a nanometre scale are often required. For the aforementioned applications, solutions can be found in the plethora of architectures of organic molecules on inorganic surfaces [1].

The organic-inorganic interfaces are of enormous importance for novel functional materials for applications such as superomniphobic [2] and heterogeneous [3] or enantioselective [1] catalyst surfaces, electronic [4, 5] and microfluidic devices [6], and for the functionalization of nanoparticles [7] and carbon nanotubes [8]. Well-ordered thin organic layers have been shown to enhance the mechanical [4], thermal [9], and adhesive [4, 10–12] properties on various substrates. These types of coatings are typically fabricated with methods that employ the self-assembly processes between the organic molecules and the substrate surface.

Organofunctional surface layers on inorganic substrates are especially important in applications, where the inorganic material is in contact with biological substances. Biocompatibility of a variety of materials is currently well-known. The driving force in the research of bio-inorganic interfaces is to gain knowledge on how to introduce functional properties to the interface. For example, the materials of implants, e.g. cardiovascular stents (most often stainless steel) or teeth implants (titanium and titanium alloys), are biocompatible: they do not release harmful substances nor induce inflammation or encapsulation of the implant. These materials are not inherently biofunctional, though. By coupling specific biomolecules to the implant surface via chemically functional hybrid interfaces, the attachment of right types of cells can be induced [13]. Organofunctional interfaces have also been studied for applications such as a single-molecule detection of biomolecules [14], bioelectronics [15, 16], biomolecule binding [15–18], and antifouling surfaces [19, 20].

The properties of the organic interface layers on solid substrates depend on the interactions between the molecules and the substrate surface. Typically, for above-mentioned applications, highly ordered, densely packed monolayers of organic molecules are required. These nanomolecular layers are only a few nanometres thick. Successful nanofabrication of such layers requires thorough understanding of the interface phenomena and control over the fabrication parameters [1].

The study of amino acids and other small molecules at well-defined surfaces is important, because they are the building blocks of larger molecules, such as peptides and proteins, and thus, they provide models for understanding the interaction between the surface and larger molecules [21, 22]. The key motivation for the research has been the versatility of the surface properties that can be gained from the fabrication of nanomolecular interfaces.

In this thesis, the adsorption behaviour of trimesic acid (TMA) and glycine (Gly) on copper single crystal (Cu(100)) and organofunctional silanes (aminopropyl trimethoxysilane (APS) and mercaptopropyl trimethoxysilane (MPS)) on stainless steel EN 1.4372 was studied. The nanofabrication of these samples was conducted with physical vapour deposition (PVD) and liquid phase deposition (LPD). Photoelectron spectroscopy (PES) was the main experimental analysis method, supported by scanning tunneling microscopy (STM). The experiments were carried out at Surface Science Laboratory, Tampere University of Technology and at the MAX IV Laboratory, a synchrotron radiation facility in Lund, Sweden.

This thesis is organized as follows: Chapter 2 introduces the phenomena related to adsorption and self-assembly of the studied organic molecules on metal and metal alloy surfaces. In Chapter 3, the PES and other analysis methods are presented. The main results are discussed in Chapter 4, and Chapter 5 comprises the summary and outlook.

2. MODIFICATION OF METAL AND METAL OXIDE SURFACES WITH ORGANIC MOLECULES

Ordered nanomolecular surface structures of organic molecules can be employed to introduce functional surface properties to metals and metal oxides [23]. By careful selection of right organic molecules and substrates, the functional properties can range from corrosion resistance and enhanced adhesion to e.g. tailored biofunctionality, enantioselective catalytic surfaces and molecular electronics.

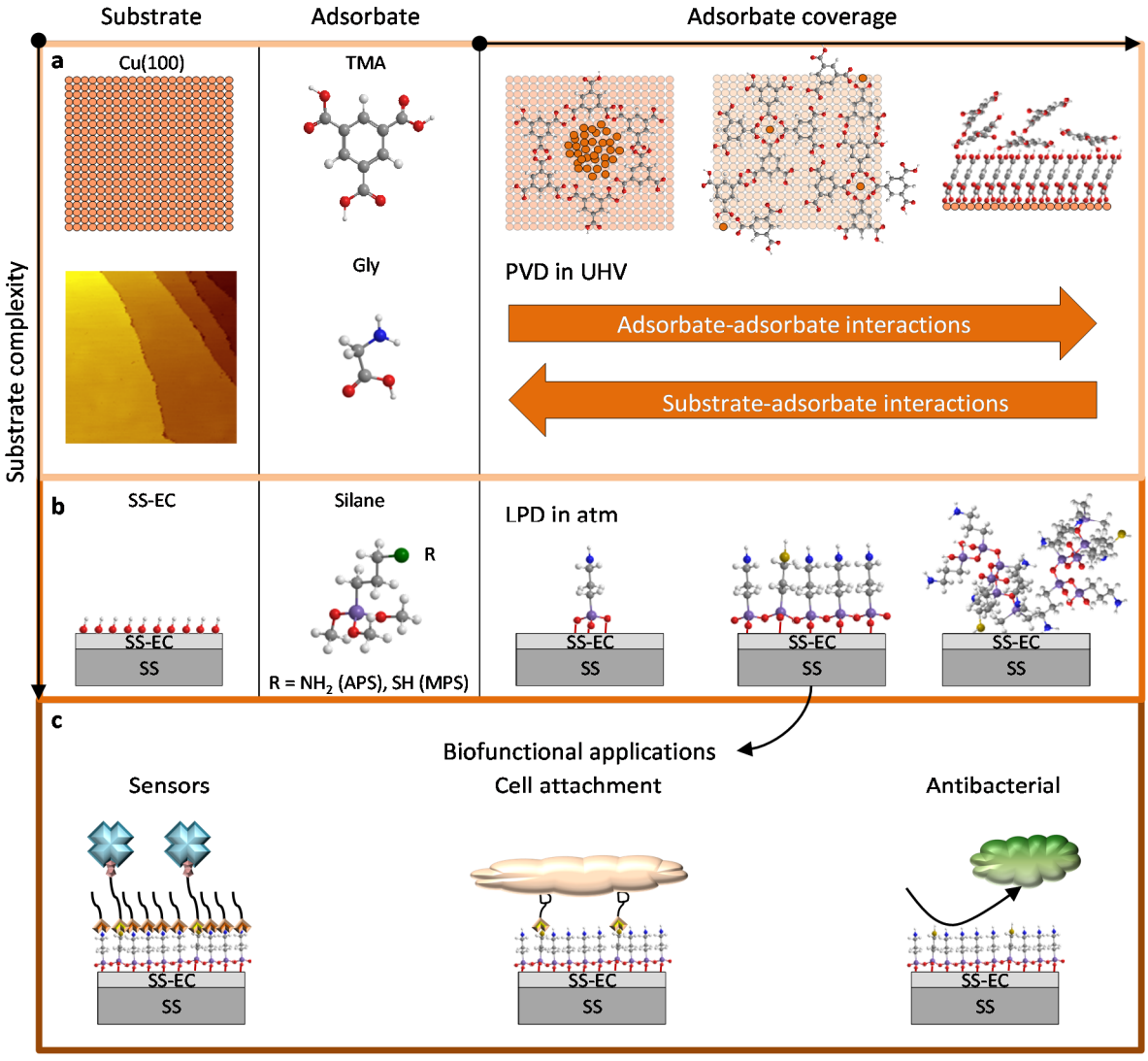

Figure 2.1. Substrates and adsorbates studied in this thesis and schematic presentations of adsorption configurations at selected coverages. (a) Adsorption of TMA and Gly on Cu(100). (b) Coadsorption of APS and MPS on electrochemically treated austenitic stainless steel (SS-EC) substrate. (c) Some potential biofunctional applications of bifunctional nanomolecular silane layers on electrochemically treated stainless steel.

Nanostructures at surfaces can be fabricated by top-down methods such as nanolithography or microcontact printing. These methods produce nanostructures in the sub 100 nm range and are analogous to traditional lithographic methods. They do not take advantage of phenomena that occur at the material interphases. The fabrication of truly nanomolecular organic structures in 0.1-10 nm scale on metal and metal oxide substrates, on the other hand, requires bottom-up approach, where the aim is to guide the assembly of the atoms and molecules through processes that are inherent in the studied system [24, 25]. In order to fabricate such structures, thorough understanding of the properties of the substrate surface, the organic molecules and deposition parameters are required [26]. With careful fabrication of nanomolecular surface layers in a highly controlled environment, new (multi)functional surfaces may be manufactured even on an industrial scale.

In this thesis, the main theme is the controlled self-assembly of small organic molecules on metal and metal alloy surfaces. The scope of the thesis is illustrated in Figure 2.1. It exhibits the studied substrates, adsorbates and possible future applications. The adsorption of two carboxylic acids, trimesic acid (1,3,5 -benzene tricarboxylic acid, $C_6H_3(COOH)_3$) and glycine (2-aminoacetic acid, NH_2CH_2COOH) on Cu(100) in ultra high vacuum (UHV) is discussed in Chapter 2.2 (Figure 2.1 (a)). Functionalization of electrochemically treated stainless steel (SS-EC) surfaces with organofunctional silanes aminopropyl trimethoxysilane ($NH_2(CH_2)_3Si(OCH)_3$) and mercaptopropyl trimethoxysilane ($SH(CH_2)_3Si(OCH)_3$) by liquid phase deposition (LPD) is presented in Chapter 2.3 (Figure 2.1 (b-c)).

2.1 Self-assembly

Self-assembly is a process where the constituents (atoms, molecules) spontaneously form supramolecular structures in 3D (in solution) or in 2D (at the surface). Self-assembly processes are important e.g. in the formation of lipid membranes of cells and protein folding and, therefore, are crucial for life [27]. The success of self-assembly depends on 1) the components in the system, 2) the interaction of the components, 3) reversibility, 4) the environment and 5) mass transport [27]. For self-assembling structures at surfaces, there are always at least two components: the adsorbate (i.e. the molecule) and the substrate. Even minor changes in the components may lead to significant differences in the resulting self-assembled structures [1]. The interactions of the components in the initial stages of the self-assembly are typically non-covalent (van der Waals, Coulomb interactions, hydrogen bonds

and hydrophobic interactions, etc.)[26]. In many cases, the self-assembly processes at surfaces lead to covalent or coordination bonding after the molecular constituents have self-organized at the surface. Reversibility is required as the constituents must be able to adjust their positions in the self-assembly process. The environment, especially the interface in 2D self-assembly, plays an important role. Mass transport, i.e. the mobility of the molecules, is required for the self-assembly to occur. The free energy minimization during spontaneous self-assembly leads to stable self-assembled systems in the equilibrium conditions [28]. Although self-assembly is spontaneous, the fabrication of nanomolecular surface coatings via self-assembly processes requires a deep understanding of the surface and interphase phenomena and substrate-adsorbate interactions, as well as, the deposition parameters.

Self-assembled monolayers (SAMs) of thiol (SH) terminated hydrocarbon molecules on gold are the most investigated organic systems on metal surfaces, as thiol chemistry provides a relatively straightforward way of creating densely packed monolayers of organic molecules on a noble metal surface. Thiol SAMs are based on the strong affinity between Au and thiol terminus of the adsorbing molecule. Fabricating SAMs or submonolayer organic surface structures on transition metal surfaces, which readily oxidize in atmospheric conditions, is a more complicated task than preparing thiol SAMs on noble metal surfaces. Whereas thiol-SAMs on Au may be fabricated in the liquid phase in atmospheric conditions, the preparation of nanomolecular organic structures on transition metals, such as Cu, require ultra-high vacuum (UHV) conditions. In UHV, the substrate surface can be kept in the metallic state and clean of impurities for long periods of time prior to the deposition of organic adsorbates, typically by physical vapour deposition (PVD).

On the other hand, SAMs can be fabricated on oxide surfaces in ambient conditions. Organofunctional silanes are a group of molecules that are most commonly used for the fabrication of SAMs on oxide surfaces in atmospheric conditions. The silanes bond with each other and with the surface creating superior stability but are more complex to fabricate than SAMs of thiolated molecules on noble metals [23].

2.2 Small organic molecules on single crystal metal surfaces

The surface architectures of the adsorbates (A) on the substrate (S) surface are governed with substrate-adsorbate (S-A) and adsorbate-adsorbate (A-A) interactions. Typically in

chemisorption, the S-A interactions are stronger than A-A interactions, whereas in physisorption, the S-A interactions are weak. Still, for long-range ordering of chemisorbed species, the A-A interactions dominate the long-range ordering [29]. The A-A and A-S interactions depend on the adsorbate and substrate properties and the adsorbate coverage. At submonolayer coverages, the adsorption configurations are governed by S-A and A-A interactions, whereas when the adsorbate coverage exceeds monolayer coverage, the S-A interactions are limited and A-A interactions determine the adsorbate configuration. In many cases, the molecules that adsorb after monolayer coverage exhibit little or no ordering unless the molecules readily react with each other. This indicates, firstly, that the substrate surface properties are crucial in fabricating nanomolecular surface structures. Secondly, the surface properties affect the molecule orientation only at a short range perpendicular to the surface plane (length of the adsorbate).

Physisorbed adsorbates interact with the substrate with dipole-dipole interactions, whereas chemisorbed molecules form stronger bonds (covalent, ionic or coordination) with the surface. In many cases, initially physisorbed adsorbates bond covalently to the substrate when additional energy is provided. Typically, this can be achieved by thermal activation upon annealing [Papers I-IV]. The annealing temperature must be chosen carefully in order to avoid the dissociation of the adsorbates, which often leads to the desorption of the adsorbate fragments or molecules.

2.2.1 Cu(100) single crystal substrate

Copper is a transition metal with a face-centred close-packed crystal structure. Single crystal Cu(100) was chosen as a substrate for the adsorption studies of TMA and glycine. The Cu(100) surface can be considered atomically flat. Still, the (100) surface has three different binding sites for adsorbing atoms or molecules as shown in Figure 2.2 (a) [29, 30].

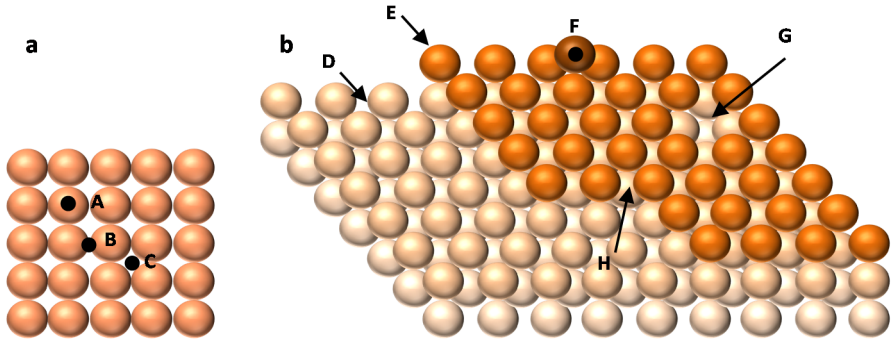

Figure 2.2 (a) Binding sites on Cu(100) surface: (A) top site, (B) bridge site, (C) hollow site. (b) Surface defects on Cu(100) surface: (D) terrace, (E) step edge, (F) adatom, (G) vacancy, (H) kink. (Adapted from references [29], [30].)

The single crystal surfaces also exhibit defects, such as adatoms,vacancies and step edges (Figure 2.2 (b)) [29, 30]. These surface defects may act as initial adsorption sites for molecules. Thus, the density of the surface defects affects the adsorption processes in the initial stages of the adsorption. The density of the defects may be controlled for example by the temperature of the substrate [Paper I].

2.2.2 Adsorption of trimesic acid and glycine

Benzene (C_6H_6), the simplest of aromatic hydrocarbons, is known to obtain a flat-lying orientation (benzene ring parallel to the surface) on various single crystal surfaces via π-π interactions [29]. Trimesic acid, a trivalent carboxylic acid derivative of benzene, on the other hand, binds to the surface via carboxyl (COOH) groups. The rigid aromatic ring and three symmetrically positioned COOH groups contribute to the adsorption configurations. The TMA may interact with each other via H-bonds at low temperatures around 130 K [31] (see Figure 2.3 (a)) or bind to a transition metal surface via coordination (Figure 2.3 (b)) or surface covalent bonds (Figure 2.3 (c-d)). Aromatic carboxylic acids on single crystal surfaces have gained a lot of research interest as they tend to form highly organized, often long-range networks of organic molecules on transition metal surfaces [32–36].

Carboxylic acids are known to bond to single crystal surfaces via a deprotonation reaction of the carboxyl group resulting in surface bound carboxylates at temperatures around 300 K [1, 31]. For TMA, the deprotonation reaction can be written as:

$$C_6H_3(COOH)_3(g) \leftrightarrow C_6H_3(COOH)_{3-x}(COO^-)_x(ads) + xH^+\,(des) \qquad (2.1)$$

If the molecule has more than one carboxyl group, the degree of deprotonation, D, can be used to evaluate the surface orientation of the adsorbates. D is determined as

$$D = \frac{COO^-}{COO^- + COOH}. \qquad (2.2)$$

Fully deprotonated TMA (D=100%) forms surface covalent or coordination bonds via all three carboxylate groups and thus is lying flat on the substrate. Figure 2.3 (b) illustrates 2D metallo-organic coordination compounds of trapped Cu atom surrounded by four flat-lying TMA molecules. Bonding via one or two COOH group(s) (D is 33% or 67%, respectively) leads to upright or tilted surface orientation (Figure 2.3 (c) and (d)). For physisorbed molecules D = 0%.

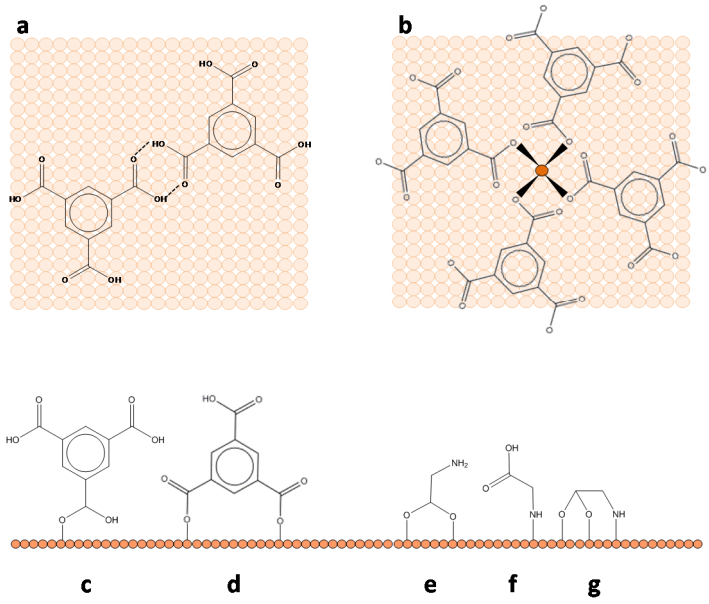

Figure 2.3. Schematic illustrations of some surface interactions of TMA and Gly on Cu(100). (a) Physisorbed TMA molecules and H-bond (dashed line) formation between carboxyl moieties of the TMA molecules. (b) Coordination bonding (black wedge) between O in TMA and Cu adatoms forming 2D metallo-organic coordination compound $[TMA]_4Cu$. Possible bonding arrangements for TMA (c) monodentate via one carboxylate group (d) two monodentate carboxylate bonds and for glycine via (e) bidentate via carbonyl and hydroxyl groups (f) monodentate via amino group (g) tridentate via all three groups.

Glycine is the simplest and only achiral amino acid. The chemical form of glycine varies between acidic (NH_2CH_2COOH), anionic ($NH_2CH_2COO^-$), cationic ($NH_3^+CH_2COOH$) and zwitterionic ($NH_3^+CH_2COO^-$) depending on the environment. In gas phase amino acids are typically in acidic form, and in solid form they are zwitterionic [1], whereas anionic and cationic forms are present in solutions and depend on the pH of the solution. At the surface,

the chemical form depends on the substrate properties and coverage [1]. Glycine may bind to Cu surface via both carboxylic acid and amino termini under certain conditions (Figure 2.3 (e-g)) [Paper II, 1, 37–39].

Chirality is a geometric property, which states that a chiral object is not superimposable on its mirror image. Both the adsorbate and the substrate may be either chiral or achiral. Significantly, under right conditions the adsorption configurations of achiral molecules on achiral single crystal substrate may exhibit chiral properties [ref. [1] and the references therein]. The adsorption studies of Gly have revealed homo- and heterochiral surface phases on Cu(100) [Paper II, 38–40]. One of the factors that affect the chirality at the surface arises from the flexibility of the molecule.

2.2.3 Potential bioapplications

The adsorption studies of TMA and Gly on Cu(100) do not provide direct solutions for biotechnological applications. Still, it is imperative that these types of adsorption systems are studied for a deeper understanding about the nanoscale surface phenomena. When the surface phenomena are comprehended, the knowledge can be used to design functional surface structures that work as single-molecule sensing devices, nano-bio interfaces or heterogeneous catalysis surfaces [28]. The adsorption behaviour of amino acids on single crystal surfaces is a prerequisite to understanding the adsorption of peptides and proteins [22]. Enantioselective catalysis is of enormous importance in e.g. pharmacology and toxicology because, in many cases, the enantiomers of a chiral molecule have differences in biological activities [41].

2.3 Chemical modification of stainless steel with nanofabricated bifunctional silane overlayers

From the industrial and commercial point of view, nanomolecular surface layers that can be fabricated cost-effectively and on an industrial scale in atmospheric conditions are more feasible than studies of small molecules on single crystal surfaces. Liquid phase deposition provides a relatively simple way to fabricate nanomolecular layers on metal and alloy oxide substrates.

Stainless steel is an affordable and mechanically viable material for many applications. The surface oxidation and subsequent formation of a few nanometres thick native oxide layer of stainless steel improves the material properties of the alloy, as the native oxide layer protects the alloy from corrosion and is self-healing.

Organofunctional silanes are a group of molecules that are widely used in coatings on various oxide surfaces, such as SiO_2 [42–47], glass [48], zirconia [49] polymers such as poly(dimethylsiloxane) (PDMS) [6, 50] and metals and alloys, such as Al [51], Ti [12, 52, 53], NiTi [54], Zn [10, 55] and stainless steel [17, 19, 56–63], as they readily self-assemble on oxide surfaces in right conditions. Silanes are used in thick coatings as well as monolayer-type layers (< 1-10 nm). The thicker silane coatings are typically used as adhesives [50], corrosion protection [63] and fillers [49], whereas the monolayer-like coatings are more viable for purposes that require more controlled functionality [Papers III and IV, 61]. The monolayer silane coatings are often used as an intermediate layer between the inorganic substrate surface and functional molecules [4, 9]. The organofunctional silanes typically have a structure of R-spacer-$Si(X)_3$, where R is the organofunctional group, and a spacer is typically a short CH_2 chain (3-12 C atoms) or a longer polymer chain, such as polyethylene glycol (PEG). X is the hydrolysable group, most often methoxy (OCH_3), ethoxy (OC_2H_5) or chloride (Cl^-).

2.3.1 Properties of APS and MPS

Aminopropyl trimethoxy- (APS) [6, 10, 15, 42, 50, 56, 57, 64, 65] and –triethoxysilanes (APTES) [15, 16, 19, 50] are probably the most investigated organofunctional silanes. Aminofunctionalized surfaces can be widely used in several applications [66]. Aminoterminated silanes have been used to promote adhesion between a substrate and carbonyl containing polymers [50, 60]. Also, a wide range of biomolecules can be coupled to surface amino groups with for example n-succinimidyl ester (NHS) or imidoester terminated molecules [16]. Another widely studied silane is thiol (SH) terminated mercaptopropyl trimethoxysilane (MPS) [4, 6, 7, 9–11, 45, 50, 55, 67]. MPS has been studied for coupling oxide surfaces with noble metal surfaces [4, 9, 55] and for other adhesive purposes [10]. Thiolated surfaces can also be used to covalently bind maleimide (MAL) terminated molecules [Paper IV].

The APS and MPS molecules are similar in size, density and molecular weight. The aim of the research conducted for this thesis is to incorporate MPS molecules in an APS matrix with controlled thiol density and monolayer configuration. Hence, the APS/MPS overlayer provides a chemically bifunctional organic interface on inorganic substrate, where the thiol and amino termini of MPS and APS, respectively, exhibit specific binding sites for (bio)functional molecules with a controllable spatial distribution.

2.3.2 Silanization via liquid phase deposition

Typically, the silanization is performed as a liquid deposition [12, 42, 49, 60, 61, 64], but other methods, such as vapour deposition [44, 47, 51, 54], plasma [42, 68] and sol-gel [63], [68] have been reported. The silanization reaction pathways are typically reported as a three-step process: 1) hydrolysis, 2) condensation in solution or at the surface and 3) covalent bond formation upon annealing [12, 56, 57, 65, 69]. In the following reaction equations, the reactions of APS and MPS are presented (R=NH_2, SH, x=0-3, y=0-3). Firstly, in a hydrolysis reaction, the X groups are cleaved and silanols (R-spacer-$Si(OH)_3$) are formed in the presence of water.

Hydrolysis *(sol)*

$$R(CH_2)_3Si(OCH_3)_3 + H_2O \leftrightarrows R(CH_2)_3Si(OCH_3)_2(OH) + CH_3OH \quad (2.3)$$

$$R(CH_2)_3Si(OCH_3)_2(OH) + H_2O \leftrightarrows R(CH_2)_3Si(OCH_3)(OH)_2 + CH_3OH \quad (2.4)$$

$$R(CH_2)_3Si(OCH_3)(OH)_2 + H_2O \leftrightarrows R(CH_2)_3Si(OH)_3 + CH_3OH \quad (2.5)$$

Under optimal conditions, the hydrolysis proceeds to fully hydrolyzed molecules, but also partially hydrolyzed molecules (R-spacer-$Si(X_{3-n})(OH)_n$, n=0…3) may take part in the following reactions. The rate of the hydrolysis reaction is governed by the amount of water in the hydrolysis solution [57], pH [50, 57], temperature [70] and the silane species. Depending on the nature of the X, either alcohols (CH_3OH, C_2H_5OH) or HCl are formed in the reactions.

In the second step, in solution, the molecules either react with each other and form siloxane bonds (Si–O) or adsorb on the substrate surface where siloxane bonding also occurs. In the

solution phase, the condensation of the silanols to oligomers is governed by silane concentration, pH and time. The reaction may proceed to the polymerization of silanes, which leads to 3D siloxane clusters.

Condensation *(sol):*

$$R(CH_2)_3Si(OCH_3)_x(OH)_{3-x}(sol) + R(CH_2)_3Si(OCH_3)_y(OH)_{3-y}\ (sol) \leftrightarrows$$

$$R(CH_2)_3Si(OCH_3)_x(OH)_{2-x} - O - (OH)_{2-y}(OCH_3)_ySi(CH_2)_3R\ (sol\ ) + H_2O(sol) \quad (2.6)$$

In the presence of hydroxyl rich solid substrate, the silanols adsorb to the surface via hydrogen bonds between the silanol and surface OH groups either as monomer, oligomers or polymers. This is a crucial step considering the monolayer formation. In the optimal situation, the adsorbing entities orient themselves upright (R pointing outwards) when hydrogen bonds between the surface and the molecules are formed.

Adsorption (ads)

$$R(CH_2)_3Si(OCH_3)_x(OH)_{3-x}(sol) + \ xMOH(s) \xrightarrow{heat}$$

$$R(CH_2)_3Si(OCH_3)_x(O)_{3-x}M(ads) + xH_2O(des) \quad (2.7)$$

The exposure time of the silanized surface to the silane solution must be optimized to obtain a densely packed silane surface configuration, but to avoid the cluster formation in the solution. When the sample is exposed to the silane solution all the phenomena mentioned above may occur simultaneously [71].

In the final step, the solution is rinsed off and the sample is dried and often annealed at elevated temperatures (60-100 °C). Annealing leads to covalent bond formation between the surface and silanols [57].

Figure 2.4 illustrates different bonding possibilities of APS, MPS and APS/MPS on stainless steel. If the hydrolysis is incomplete, unhydrolyzed or partly hydrolyzed silanes may adsorb in random orientation. If silane species adsorb as condensed clusters or polymers, the surface loses its ability to orient the silane molecules and disordered surface structures are formed. The bonding possibilities are presented in more detail in Paper III and in Chapter 4.3. In order

to fabricate silane monolayer, a low concentration of silanes, typically around 0.1- 1.0 v-% of hydrolysis solution, leads to good results [56].

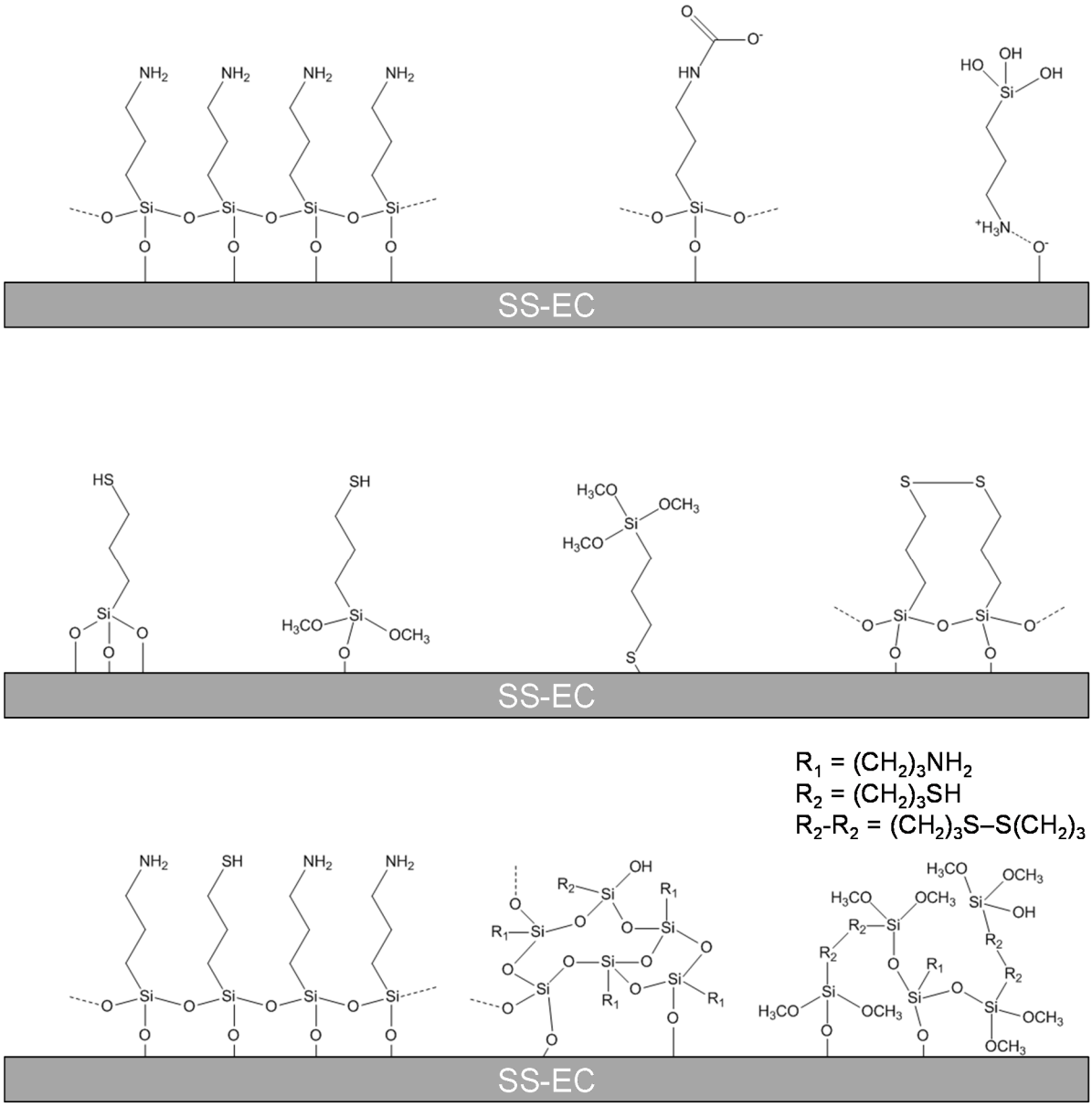

Figure 2.4. (Top) APS: highly ordered and up-right oriented APS monolayer, carbamate (NHC=O) terminated silane due to reaction with NH_2 and CO_2, up-side down oriented APS; (middle) MPS: tridentate Si–O bonding, partly hydrolyzed, up-side down oriented and MPS dimer with a disulphide bond; (bottom) APS/MPS: ideal bonding for bifunctional APS/MPS monolayer, clustering induced by condensation, clustering induced by incomplete hydrolysis. Modified from Paper III.

The LPD silanization procedures can roughly be divided to two categories. A relatively rapid (some minutes) hydrolysis and exposure in aqueous solutions [Papers III, IV,19, 56, 72] or a very long exposure in anhydrous solutions where the water at the substrate-air interface in ambient conditions works as a catalyst for the hydrolysis [50, 58, 73]. For small silanes, with a short spacer, the former is often chosen.

If different silane species are coadsorbed from the same hydrolysis solution, it must be taken into account that the reaction rates for hydrolysis and condensation are strongly dependent on the properties of the silanes [Papers III and IV]. Hence, the silane surface ratio may be significantly different from silane solution ratio, although identical solution and surface ratios for mixtures of alkyltrichorosilanes have been reported [74, 75].

2.3.3 Role of surface hydroxylation

The substrate surface hydroxyl concentration plays an important role in the silanization process. The initial H-bond formation at the substrate-hydrolysis solution interface orients the adsorbed silane molecules with the organofunctional group outwards. Lack of surface hydroxyls induces clustering of the silanes [5, 56, 74]. Random orientation is not so detrimental in thick (μm range) silane coatings as the molecular orientation at the outer interface is random in any case. Still, the substrate hydroxyl concentration determines the number of bonds between the silanes and the substrate [76]. For applications that employ monolayer silane coatings, the substrate hydroxylation is of utmost importance. The stainless steel oxide surface is not inherently sufficiently hydroxylated [56].

The enrichment or fabrication of the surface OH groups is typically performed for all substrates by immersing the sample in one or several harsh oxidizing solvents [18, 45] such as Piranha solution (a mixture of strong sulphuric acid and hydrogen peroxide) [5, 42, 52, 59, 76]. The hydroxylation can also be performed by electrochemical (EC) [56] or plasma [50, 62] treatments or atomic layer deposition [61].

2.3.4 Bifunctional silane overlayer for biofunctional applications

In many cases, the functionality of nanomolecular silane layers is due to sandwich-like deposition of functional layers of other molecules on top of the silane layer at the organic-inorganic interface (see Figure 2.1 (c)). In bioapplications, biomolecules are coupled to the silane surface with covalent bonding between silane organofunctional groups and the biomolecule. The correct orientation of and the spatial availability of the silane organofunctional groups is therefore crucial. This is especially the case in bifunctional silane layers, where the aim is to couple different molecules to the silanes. These bifunctional surfaces can be biofunctionalized by covalently coupling biomolecules to the thiol termini of

MPS, while amino groups of APS are coupled to molecules that enhance the antifouling surface properties. For many biofunctional applications such as biosensors or implant surfaces, the spatial distribution and orientation of biomolecules at a surface is the key parameter that determines the functionality.

Bifunctional silane coatings, that is, nanomolecular overlayers of two different silanes have been studied most often for biofunctional applications. Slaney *et al.* have studied carbohydrate functionalized silanes mixed with polyethylene glycol (PEG) silanes on SiO_2 coated SS [61]. Schartner *et al.* report bifunctional silanization of Ge for protein immobilization [18]. Shirlcliff *et al.* introduce a method to immobilize DNA to silica substrate via bifunctional silane monolayer [77]. Matinlinna *et al.* have mixed various silanes with a cross-linking silane *bis*-1,2-(triethoxysilyl)ethane in order to enhance the bonding between silica coated dental implant and resin cements [12, 49] and to prevent biofilm formation [53].

3. EXPERIMENTAL METHODS AND DATA ANALYSIS

The experimental work in this thesis was conducted at the Surface Science Laboratory, Tampere University of Technology and at the synchrotron radiation facility MAX IV Laboratory, Lund, Sweden. The experimental work and the surface analysis methods related to this thesis are schematically presented in Figure 3.1.

The sample preparation steps for *in situ* samples (trimesic acid and glycine on copper) and *ex situ* samples (silanes on stainless steel) are illustrated in the blue frame on the top. Both sample preparation procedures include substrate surface cleaning or modification treatments prior to organic molecule deposition by physical vapour deposition for TMA and Gly and liquid phase deposition for silanes. The sample preparation procedures are described in more detail in Chapter 3.1.

The main surface analysis method in this work was photoelectron spectroscopy (PES). The principle of PES and other related issues are presented in Chapter 3.2, whereas the analysis of PES data is described in Chapter 3.3. The information gained from the PES experiments was used to determine and quantify the surface elements and their chemical states (Chapters 3.3.1 and 3.3.2). SR-PES was employed in the non-destructive depth profiling (Chapter 3.3.3), and the surface morphology was determined with inelastic electron energy background analysis (Chapter 3.3.4). The different kinds of information that can be gained from the PES data are illustrated in the green frame in Figure 3.1. Chemical derivatization, a method for studying the reactivity of surface functional groups is introduced in Chapter 3.3.5.

Chapters 3.4 and 3.5 briefly introduce scanning tunneling microscopy (STM) and density functional theory (DFT), respectively. STM was used to gain information on the TMA and Gly adsorption configurations combined with DFT calculations with the latter.

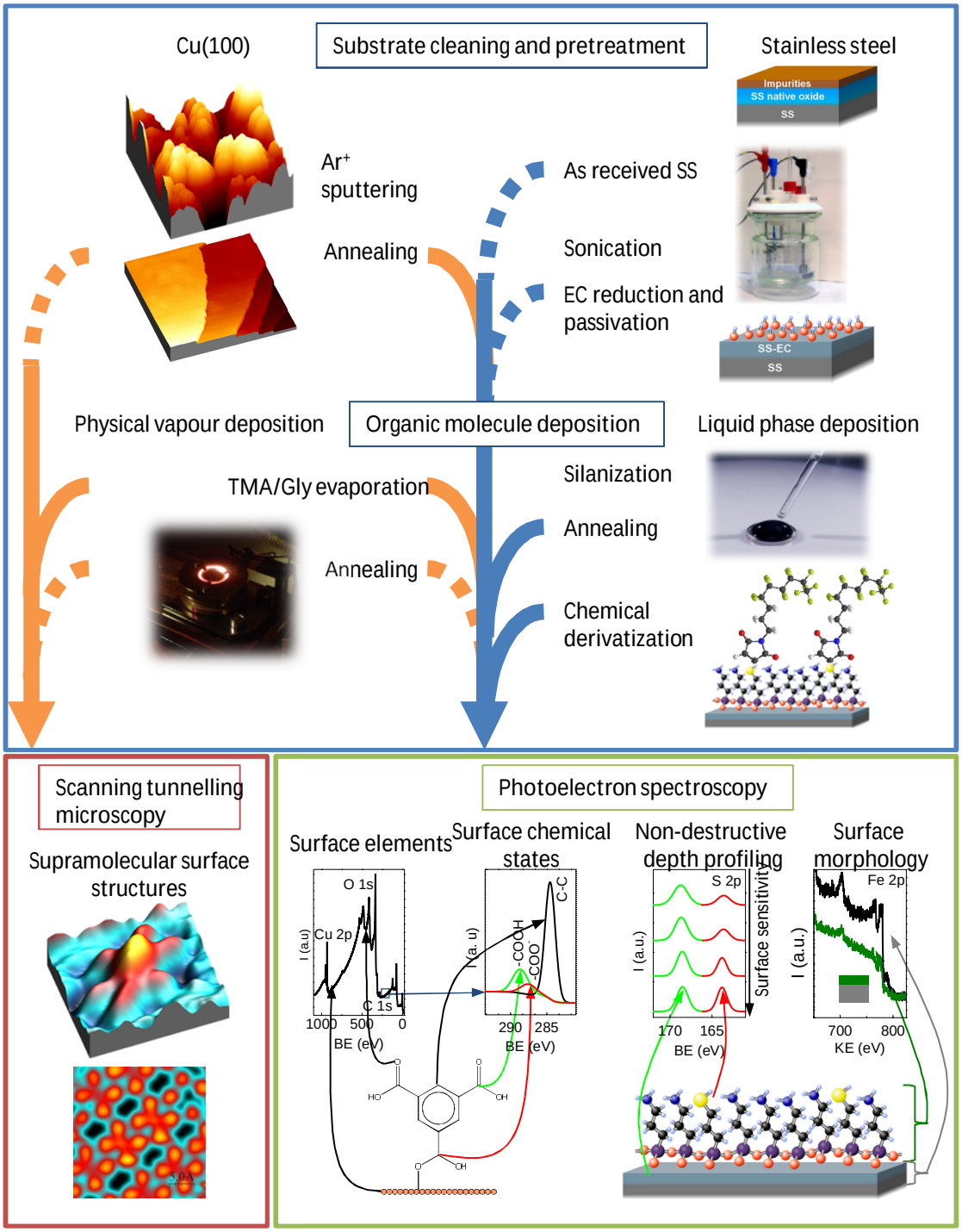

Figure 3.1. Fabrication procedures for samples (blue frame). Arrows indicate sample preparation stages where PES (blue frame) and STM (orange frame) were employed during sample preparation routinely or when required (dashed lines).

3.1 Sample preparation

In situ PVD was employed as a deposition method for TMA and Gly nanostructures on Cu. PVD provides a relatively simple and reproducible method for studying nanomolecular systems in detail in the ultra-pure environment of the UHV. In PVD, the deposited substances are heated and the substrate is brought under the flux of the evaporating molecules. The adsorbate coverage depends on the temperature and the partial pressure of the molecule, the exposure time and the geometry of the evaporating chamber. After the deposition, the sample can be subjected to further treatments and surface analysis without exposure to atmospheric conditions. The substrates and chemicals used in the experiments are presented in Table 3.1.

Table 3.1. Substrates and chemicals used in the experimental work.

	***In situ* PVD**	***Ex situ* LPD**
Adsorbate	TMA, purity 98% (Alfa Aesar) Glycine, purity 99.5% (Alfa Aesar)	APS, purity >97% (Sigma-Aldrich) MPS, purity >95% (Sigma-Aldrich)
Substrate	Cu(100), purity 6n, (Metal Crystals Oxides Ltd)	EN 1.4372 (ASTM-201) (JaloteräsStudio)
Substrate pre-treatment	-	Sulphuric acid (H_2SO_4), 95-98% A.C.S. reagent, Sigma-Aldrich
Chemical derivatization	-	*N*-(4,4,5,5,6,6,7,7,8,8,9,9,9-Tridecafluoro-nonyl)maleimide, MAL-F, purity >97% (Sigma-Aldrich) Dimethyl sulphoxide, DMSO, purity >99.9%, Sigma Tris(carboxyethyl) phosphine hydrochlorine solution, TCEP, Sigma

The APS and MPS silanes were deposited by an *ex situ* liquid phase deposition. The LPD is a fast and reproducible deposition method and suitable for the fabrication of nanomolecular surfaces with industrial interest, as the method is easily scalable to production.

3.1.1 *In situ* fabrication of TMA and Gly nanostructures on Cu(100)

The Cu substrate cleaning procedure is described in detail in Paper I. Briefly, the Cu(100) substrate was cleaned in UHV by Ar^+-ion sputtering (electron beam voltage E_B = 2.0 kV, p_{Ar} = 2.0×10^{-6} mbar, I_{target} =15 μA) followed by electron beam annealing at 700 K for 10 min (E_B = 600 V, p < 1×10^{-8} mbar). The cleaning procedure was followed by PES experiment to determine that the surface was free of C and O contamination.

Powders of either TMA or Gly were sealed in a glass tube, which was connected to the UHV system. The tube was heated to ~460 K for TMA and ~350 K for Gly. The Cu(100) substrate was exposed to the TMA or Gly flux for varied lengths of time (5-600 s) in order to obtain samples with different adsorbate coverages. The temperature of the Cu(100) was ~320 K during the deposition. The sample was then studied with PES and STM. Some samples were annealed after adsorbate deposition at varied temperatures. The stoichiometric analysis of the surface concentrations derived from the PES data revealed that both TMA and Gly remain intact upon the deposition.

3.1.2 *Ex situ* liquid phase deposition of silanes on stainless steel

EN 1.4372 (ASTM-201, Fe-18Cr-6Mn-4Ni) austenitic stainless steel grade was used as substrate for silanization. It is an inexpensive steel grade for a variety of purposes, ranging from kitchenware to architectural structures. Silanization treatments have been studied at the Surface Science Laboratory also for other steel grades, Fe-18Cr-7Mn-3Ni [56] and for ASTM 316L [72], the latter of which is a steel grade approved for medical implants and surgical instruments. The composition of the stainless steel bulk does not influence the silanization process as long as the hydroxylation of the surface is sufficient. The bulk composition of EN 1.4372, as reported by the manufacturer, is listed in Table 3.2. The steel was electrochemically polished by the supplier. The electrochemical polishing removes surface impurities, decreases surface roughness in the micrometre scale and affects the composition of the surface oxide layer [72]. After electrochemical polishing, trace impurities such as Ca, P, Mg and Na were detected on the sample surface as shown in Table 3.2 (as received SS).

Table 3.2. Elemental bulk composition of EN 1.4372 [78] and elemental surface compositions of as received and EC treated EN 1.4372 coupons determined by XPS (hν = 1486.6 eV). Elements in the APS and MPS are indicated in italics. [Supplementary data of Paper III]

Sample (at-%)	**Fe**	**Cr**	**Mn**	**Ni**	***C***	***N***	***O***	***Si***	***S***	**Ca**	**P**	**Na**	**Mg**
EN 1.4372 (ASTM-201)	70.2	18.1	6.5	4.2	*0.2*	*0.8*	-	-	-	-	-	-	-
as received SS	4.5	2.4	0.3	-	*7.7*	*1.4*	*60.4*	-	*1.0*	8.2	12.1	0.6	1.4
SS-EC	13.5	13.2	2.4	1.2	*8.0*	*1.8*	*57.4*	*1.1*	*1.4*	-	-	-	-

The electrochemical (EC) treatment consists of a reduction of the native oxide layer prior to passivation at a constant potential. It has been shown to increase the surface OH concentration [56]. The stainless steel substrates were cleaned by sonication for 10 minutes both in ethanol and deionized (DI) water. The EC treatment was performed with Autolab PGSTAT12

potentiostat/galvanostat (Eco Chemie B.V., The Netherlands). The sample was placed in a three-electrode electrochemical cell using an Ag/AgCl electrode as a reference electrode and a Pt as a counter electrode. The sample surface was then reduced in a deaerated aqueous solution of 0.1 M sulphuric acid by applying a cathodic current (i = 5 mA/cm^2) for 5 min. The passivation was conducted in the same electrolyte solution at a constant potential of E_p = -0.197 V against the Ag/AgCl electrode for 10 min. The passivated sample was rinsed with DI water and dried with N_2.

The APS and MPS were pipetted into a hydrolysis solution (1:3 EtOH:DI H_2O) simultaneously. The steel coupons were silanized by pipetting ca. 100 µl of the solution on to the sample. Both the hydrolysis and silanization times were 60 s. After silanization, the samples were dried with N_2 and annealed *ex situ* at 373 K for 10 min. In addition to APS/MPS mixtures on SS-EC, APS and MPS on stainless steel were also studied separately. The samples with APS and MPS on stainless steel are named as APS x/MPS y where x and y refer to APS and MPS solution concentrations (v-%), respectively.

3.2 Photoelectron spectroscopy

PES is a spectroscopic method that provides information of the sample surface by measuring the energies of electrons that are emitted from the surface under the irradiation of electromagnetic radiation. It provides information on the elements at the surface and their chemical states; hence, the method is also called Electron Spectroscopy for Chemical Analysis (ESCA).

3.2.1 Photoelectric effect

Photoelectron spectroscopy is based on the photoelectric effect, where the exposure of a surface to electromagnetic radiation, typically in the soft x-ray region, results in electron emission from the surface [79– 81]. The emitted electrons are called photoelectrons and their electron kinetic energy (*KE*) is given by:

$$KE = h\upsilon - BE - \phi_S, \qquad (3.1)$$

where $h\nu$ is the energy of the irradiation (h is the Planck constant, ν is the frequency), BE is the characteristic binding energy of the atomic orbital where the electron originates from, and ϕ_S is the spectrometer work function. The photoemission process is shown in Figure 3.2 (a). As a photoelectron is emitted, a hole in a core level is created. The core hole is rapidly filled with an electron from higher energy level. The energy which is released as the hole is filled may be large enough for a third electron to be emitted. This electron is called an Auger electron (Figure 3.2 (b)). The core hole may also be filled in an x-ray fluorescence process, where an electron from higher energy level emits an x-ray photon during transfer to lower energy level [81].

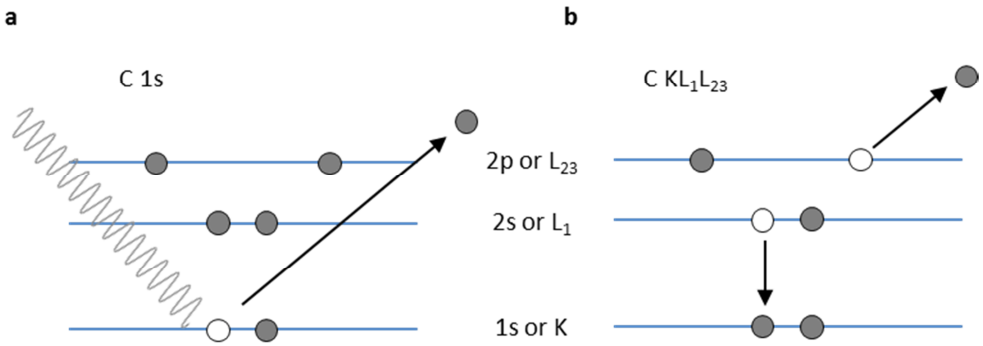

Figure 3.2. (a) The photoemission and (b) Auger electron processes. Grey circles denote an electron and white circle a hole.

The Auger electron energy is given by:

$$KE = BE_A - BE_B - BE_C - \phi_S \qquad (3.2)$$

where BE_A is the binding energy of the initial hole level, BE_B the binding energy of the level from which the core hole is filled and BE_C is the binding energy of the level where the Auger electron is emitted.

The photoelectron spectrum, the intensity (photoelectron count) versus the BE can be used to determine the elements at the sample surface within a few nanometre depth. The spectrum features photoelectron peaks and Auger transitions. The photoelectron binding energy depends on the element and the transition of the emitted electron. This enables the recognition of the elements at the surface. Auger electron peaks have constant kinetic energy. Both

photoelectron and Auger peaks carry information on the chemical environment of the atom where the electron originates from (Chapter 3.3.1).

3.2.2 Surface sensitivity

The surface sensitivity of PES arises from the inelastic processes that occur between the emitted photoelectrons and the surrounding matter in the surface region. The photons penetrate into the studied material up to a few micrometres [80], but the probability of a photoelectron to leave the surface without energy loss decreases as a function of depth. The photoelectron flux for a homogenous surface is described by Beer-Lambert law:

$$I(z) = I_0(z)e^{-z/\lambda \cos\theta}. \quad (3.3)$$

I(z) is the intensity of the photoelectron flux originating at depth *z* below the surface, $I_0(z)$ is the intensity at $z = 0$, θ is the angle with respect to the surface normal and λ is the inelastic mean free path (IMFP) of the electron [79], [82]. The IMFP describes the average path length the electron travels between inelastic collisions in a scattering process. The IMFP depends on the kinetic energy of the photoelectron and, to a lesser degree, on the material parameters, such as density, molecular weight and the number of valence electrons. The *KE* dependence of the IMFP is non-linear, and the IMFP values reach minimum values with *KE* between 100…1400 eV. In photoelectron spectroscopy, this is known as the universal curve, a plot of IMFP values vs. electron *KE* [83].

The IMFP values for different materials can be calculated from TPP-2M equation by Tanuma, Powell and Penn [84]. The sampling depth in PES is the depth from where 95% of all photoelectrons emanate and is equal to $3\lambda \cos\theta$ [82]. Figure 3.3 (a) shows the decay of the photoelectron intensity as the depth increases according to Equation 3.3. The surface sensitivity of the PES information can be increased by varying the emission angle (Figure 3.2 (b)). Angle resolved PES (AR-PES) was employed in the study of TMA and Gly on Cu(100) [Papers I and II].

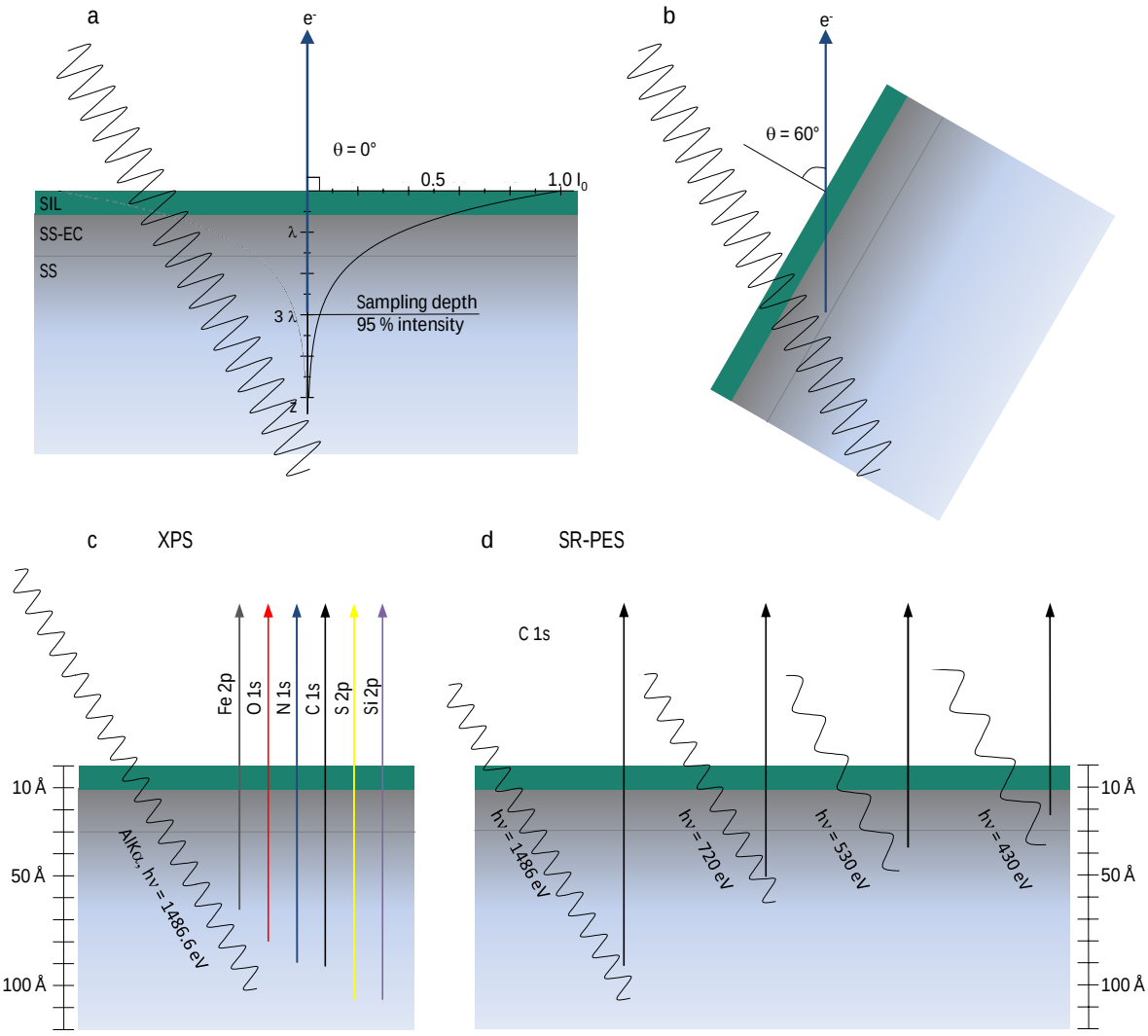

Figure 3.3. (a) Photoelectron intensity as a function on depth and the normal emission. (b) Angle resolved PES. (c) Sampling depths illustrated as the length of the arrow for iron and the elements in silane molecules in XPS with AlKα irradiation energy. (d) Different sampling depths for carbon.

In conventional XPS, the sample is irradiated with characteristic X-ray radiation, typically MgKα (1253.7 eV) or AlKα (1486.6 eV). Figure 3.2 (c) illustrates the sampling depth of Fe and the elements in silanes (H is not detected in PES). For silanized stainless steel samples, the photoelectrons from the silane layer (typically ~ 10 Å), the electrochemically treated stainless steel oxide layer (SS-EC, ~20 Å) and the metallic stainless steel below the oxide layer contribute to the photoelectron signal intensity. According to Eq. 3.1, in an XPS experiment with constant $h\nu$, electrons from different elements and transitions have different *KE*, and, thus, they originate from slightly different depths. For Gly and TMA on Cu, this does not pose a problem as the signal from the organic layer can be easily distinguished from the substrate signal. For APS and MPS on stainless steel, the analysis is more complex because the elements in silane molecules are present in the SS-EC layer and/or in the stainless

steel bulk. C, N, S and Si are present as minor alloying elements, O is a major constituent in the SS-EC, and *ex situ* samples also typically contain some C and O contamination.

3.2.3 Synchrotron radiation mediated photoelectron spectroscopy

Synchrotron radiation is produced by electrons travelling in an accelerator ring at nearly the speed of light. The synchrotron radiation has a continuous energy, ranging from soft x-rays to infrared. One of the major advantages of synchrotron radiation is the tuneable photon energy. This enables constant kinetic energy (constant IMFP or sampling depth) experiments, i.e. the photon energy can be chosen for each element to yield information from the sample at equal depths for each element [85]. In multielement samples, such as silanized stainless steel, Auger transitions from several elements hinder the choice of the constant *KE*, but it is possible to probe each element of the sample from the same region, e.g. the silane overlayer or SS-EC. The use of synchrotron also enables the non-destructive depth profiling. i.e. probing an elemental transition with different photon energies. Figure 3.2 (d) shows the sampling depths of the carbon measured with different photon energies. Another advantage of SR-PES is the increased surface sensitivity compared with conventional XPS; synchrotron radiation provides considerably increased surface sensitivity enabling more detailed analysis of the silane surface chemistry.

The synchrotron radiation also enables the optimization of the photoionization cross section, σ, i.e. the probability of a photoelectron production from the specific electronic state of a specific element [79]. The cross section of a given transition depends on the photon energy. Hence, the synchrotron radiation enables the cross section maximization/optimization and thus the detection of minor species that are not observed with conventional XPS. This applies both to minor concentrations of elements and their chemical states. Synchrotron radiation sources also have higher brilliance and higher energy resolution than XPS. The former enhances the sensitivity (signal-to-noise ratio) and the latter increases the ability of recognizing different chemical states with small *BE* difference. [86, 87].

3.2.4 Instrumentation

Photoelectron spectroscopy equipment consists of a photon source, an electromagnetic lense system, an energy analyser and an electron multiplier. In XPS, X-ray guns with Mg and/or Al Kα photon source are typically used. The emitted electrons are collected into an energy analyser with an electromagnetic lense system. Electrons, which have travelled through the energy analyser are then multiplied and counted. A computer controls the measurements and collects the data.

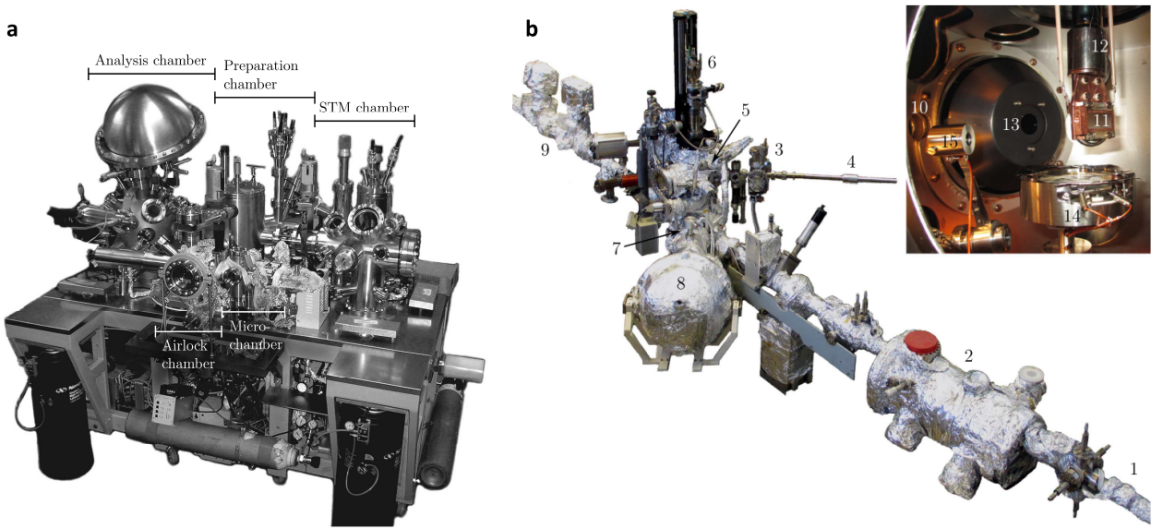

Figure 3.4. (a) The Multilab equipment at Surface Science Laboratory. The air lock chamber is for loading the samples. Also, the Gly and TMA depositions were conducted in the air lock chamber. *In situ* substrate cleaning was performed in the preparation chamber, XPS experiments were performed in the analysis chamber and the STM experiments in the STM chamber. The equipment enables sample cleaning, preparation and XPS and STM experiments without exposure to air. (b) The BL D1011 at the MAX IV Laboratory: The beamline from the synchrotron (1), Planar grating monochromator (2), load lock (3), sample transfer rod (4), preparation chamber (5), manipulator (6), analysis chamber (7), hemispherical energy analyser (8), focusing lenses and beamline to end work station. In the inset: inlet for the photon beam (10), sample and sample holder (11), lower part of the manipulator (12), inlet for the analyser lens system (13) and Partial Electron Yield detector (14) and a grid for the measurement of the photon flux. Photos by the courtesy of M. Hannula.

The PES experiments were conducted at the Surface Science Laboratory with the Multilab surface analysis system (referred as XPS) [88] and the NanoESCA spectromicroscopy system. Spectromicroscopy enables the lateral chemical mapping of the sample surface and it was used to determine the distribution of siloxane bonds and metal oxides on silanized sample using the energy filtered X-ray photoemission electron microscopy (EF-XPEEM). PES experiments were also conducted at the BL D1011 at the MAX IV Laboratory (referred as

SR-PES) [87]. The instruments are illustrated in Figure 3.4. Details of the instruments are described in Papers I-IV.

3.3 Analysis of photoelectron spectroscopy data

PES is a well-established method in the research of thin organic coatings on metal and metal alloy surfaces for a wide variety of applications. The main emphasis in the data analysis of this thesis is in the detailed understanding of the surface chemistry, A-A and A-S interactions and molecular orientation in the organic layers as a function of coverage. This Chapter focuses on the different types of information that can be obtained from the PES data.

3.3.1 Identification of surface elements and chemical states

When investigating an unknown sample, PES experiments are initiated with a measurement of a survey scan with a typical binding energy range of > 1000 eV. Survey scans are typically recorded in the constant retard ratio (CRR, also Fixed Retard Ratio, FRR) mode of the energy analyser. The CRR mode enables high elemental detectability, but is not suitable for quantification as the energy resolution of the mode depends on the photoelectron *KE*. Survey spectrum consists of photoelectron peaks of different transitions of elements and Auger transitions within the sampling depth. In Figure 3.5, survey spectra of TMA/Cu and Gly/Cu samples measured with MgKα and AlKα irradiation energies are presented, respectively. Auger transitions have constant kinetic energy and thus appear at different positions at *BE* scale when different photon energy is used. By changing the photon energy (dual anode or SR-PES), the Auger transitions can be shifted, as shown in Figure 3.5.

In a photoelectron spectrum, electrons from a certain transition of a certain element appear as a photoelectron peak. Only the electrons that have not suffered inelastic collisions between the photoionization process and have escaped from the surface contribute to the signal intensity of the photoelectron main peak. Electrons that have lost kinetic energy contribute to the background signal and appear on the higher *BE* side of the photoelectron peak.

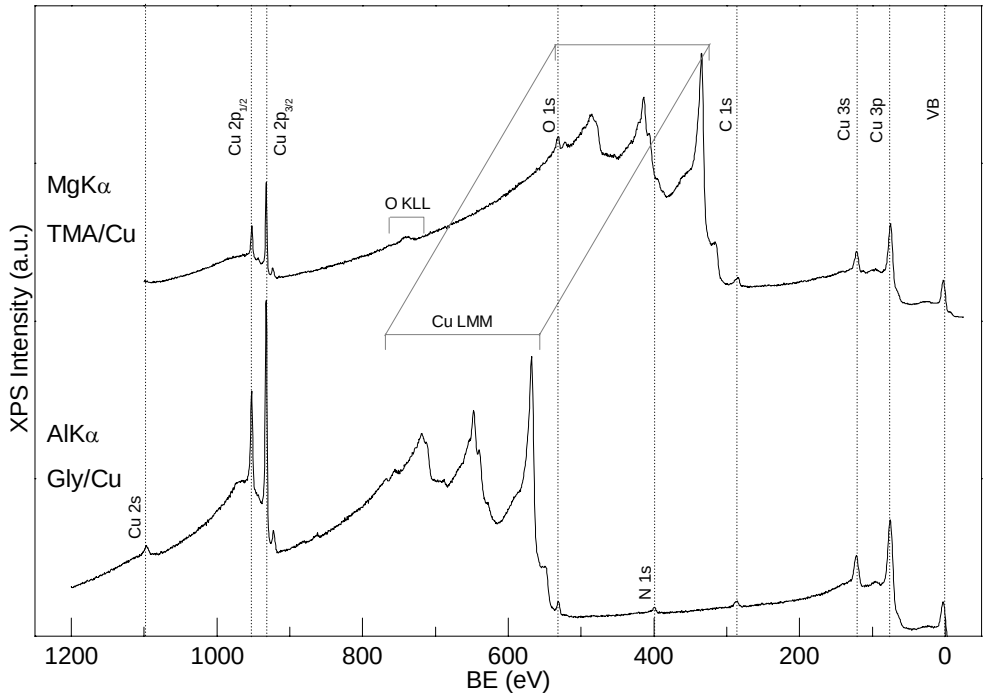

Figure 3.5. Survey XP spectra of TMA/Cu(100) (top) and Gly/Cu(100) (bottom) recorded in CRR mode. Photoelectron peaks are indicated with dashed lines.

By the measurement of the high resolution spectrum with a *BE* range of ~30 eV, a more detailed understanding can be obtained of surface chemical bonds. High resolution spectra are recorded in a constant analyser pass energy (CAE, also Fixed analyser transmission, FAT) mode. This mode has a constant energy resolution and is typically used in the recognition of the surface chemical states and in quantification.

The initial and final states of the photoelectron process can affect the *BE* and shape of the photoelectron peak. In order to determine the chemical bonding in the organic overlayers, initial stage effects are more important, as they represent changes the electrons undergo before photoemission and describe the effects induced by bonding between atoms [79]. The chemical bonds form between the valence electrons of atoms. The core level electrons do not take part in the bond formation, but their energy is altered upon binding due to changes in the electron density compared with a ground stage of an atom [79]. Initial stage effects arise from ground state polarization, inter or intra-atomic Coulombic interactions and spin-orbit splitting. Coulombic interactions are observed as *BE* shifts (chemical shift) in the photoelectron spectrum. The oxidation number and electronegativity of the neighbouring atom affect the binding energy. The *BE* shift caused by Coulombic interactions can be calculated as:

$$E_i^b = kq_i + \sum_j \frac{q_j}{r_{ij}} + E_i^{ref} \quad (3.4)$$

where E_i^b is the binding energy of an electron in the atom i, k is a constant, q_i is the charge of the atom i and q_j is the charge of the neighbouring atom j, r_{ij} is the distance between atoms i and j, and E_i^{ref} is the appropriate binding energy reference. [79, 81].

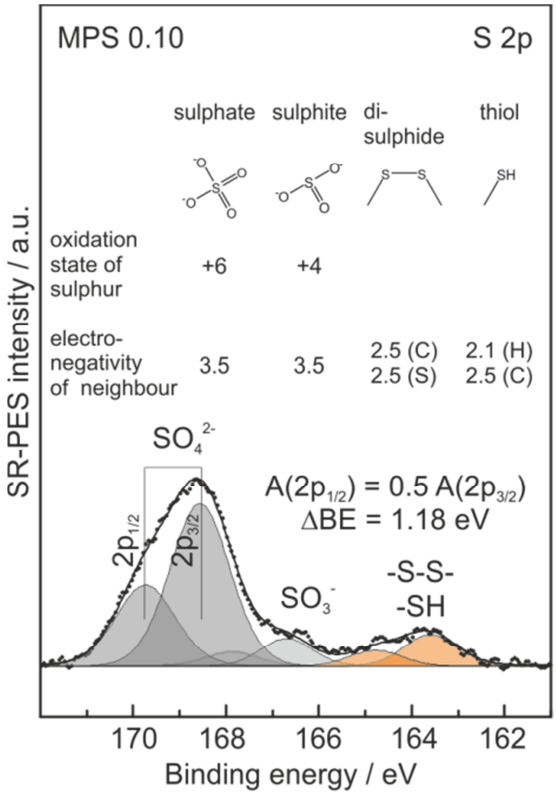

Figure 3.6. S 2p SR-PE spectrum of MPS 0.10 sample (hν = 494 eV). Molecular bonds, oxidation state and the electronegativity of the neighbouring atom for each chemical state observed in the spectrum.

The chemical shifts of sulphur in different chemical states are presented in Figure 3.6, which shows the S 2p spectrum for the MPS 0.10 sample. Three chemical states are detected. Each of these states consists of two peaks as 2p transition undergoes spin orbit splitting, the coupling of magnetic fields for orbitals with an angular quantum momentum number l >0. This is observed as a splitting of 2p into $2p_{3/2}$ and $2p_{1/2}$ peaks. The area ratio for $2p_{3/2}$ and $2p_{1/2}$ is 2:1 and the ΔBE remains the same independent of the chemical environment. [79, 81]. The chemical states in Figure 3.6 are thiol and disulphide (S–S) bonds at 163.5 eV [45, 89], sulphate ions at 168.5 eV [80] and sulphites in between [10, 11]. SH and S-S originate from the silane molecules (disulphide bonds may form between adjoining MPS molecules during

annealing [67]) and SO_4^{2-} from the sulphuric acid residue in the SS-EC. The presence of water and oxygen at a SAM surface may cause oxidation of thiols to sulphites [90].

As shown in Figure 3.6, the *BE* increases as the oxidation number of the atom and the electronegativity of the neighbouring atom increases. As the final stage effects also contribute to the photoelectron spectrum, the interpretation of the spectra is not always as straight forward as in Figure 3.6. The final stage effects are caused by the interactions between emitted photoelectrons and the surrounding matter. Intra- and interatomic relaxations caused by the core hole may contribute significantly, even to a greater extent than changes in the oxidation state [82]. Thus, reference samples, *BE* databases and literature references are important when analysing the spectra. The final stage effects also provide information on the surface. Aromatic carbon compounds (e.g. benzene and its derivatives) can be distinguished from aliphatic carbon. The shake-up process of $\pi \rightarrow \pi^*$ of an aromatic ring may be induced by a C 1s photoelectron. The KE loss of the C 1s photoelectron is observed as a small peak at +6.7 eV *BE* of the main peak [Paper I, Figure 5, [80]

In this study, the PE spectra were analysed with CasaXPS software [91]. The *BE* was calibrated to 932.7 eV for samples with Cu substrate and to 285.0 eV for aliphatic carbon for silanes on steel. The photoelectron peaks were fitted with a combination of Gaussian (70%) and Lorentzian (30%) line shapes for elements in the adsorbates. XP spectra were fitted with a Shirley background, whereas a linear background was often used with SR-PE spectra. For S 2p, the S $2p_{1/2}$ peaks were fitted with fixed parameters of *BE* difference +1.18 eV and area 0.5 × S $2p_{3/2}$ and equal Full Width at Half Maximum (FWHM). For the Si 2p spectra $2p_{3/2}$ and $2p_{1/2}$ *BE* difference is 0.60 eV and the states were not resolved in SR-PE spectra. The FWHM values for C 1s, O 1s, Si 2p and N 1s were fixed to equal for each component in a spectrum. The fitting parameters were determined from the SR-PE spectra and employed in the analysis of the XP spectra. There was no discrepancy between the XPS and SR-PES fittings except for slightly wider FHWM values for XPS, and some trace chemical states were not detected in XPS experiments.

3.3.2 Quantification

The PES data can be used to determine the surface concentration of each element and its chemical state within the sampling depth in at-%. The photoelectron intensity, *I*, of a given

transition is equal to the area of the corresponding component in a high resolution spectrum and can be written as

$$I_{ij} = KT(KE)L_{ij}(\gamma)\sigma_{ij}\int n_i(z)e^{-z/\lambda(KE)cos\theta}dz, \quad (3.5)$$

where I_{ij} is the area of the peak j from the element i, K is an instrumental constant, $T(KE)$ is the analyser transmission function, $L_{ij}(\gamma)$ is the angular asymmetry factor for orbital j of the element i, σ_{ij}, is the photoelectron cross section of the peak j from the element i and $n_i(z)$ is the concentration of the element i at the distance z below the surface [82]. Accurate determination of the parameters in Eq. 3.5 is difficult. Typically, relative surface concentrations c_x (at-%) are determined from Eq. 3.6

$$c_x = \frac{n_x}{\sum n_i} = \frac{I_x/S_x}{\sum I_i/S_i}, \quad (3.6)$$

where n_x is the number of atoms and S_x is the sensitivity factor of species x. The sensitivity factor depends on the photoelectron cross section, the IMFP, the transmission function of the energy analyser and instrumental factors.

3.3.3 Non-destructive depth profiling

The tuneable photon energy in the SR-PES enables non-destructive depth profiling [92]. As described in Figure 3.3., the sampling depth depends on the photon energy. By measuring SR-PE spectra of a single sample with many photon energies, information of the relative amount of e.g. chemical bonds at a certain sampling depth can be obtained. Figure 3.7 shows S 2p spectra of APS 0.10/MPS 0.05 sample measured with different photon energies. As the photon energy decreases (from top to bottom) and the surface sensitivity increases (due to shorter IMFP values), the thiol photoelectron signal increases in relation to the sulphate signal. Figure 3.7 also illustrates the cross section dependence on the photon energy. The signal intensities in the spectra have been normalized to equal maximum intensity of the sulphate signal. The values on the right indicate the factor by which the intensity was multiplied in the normalization.

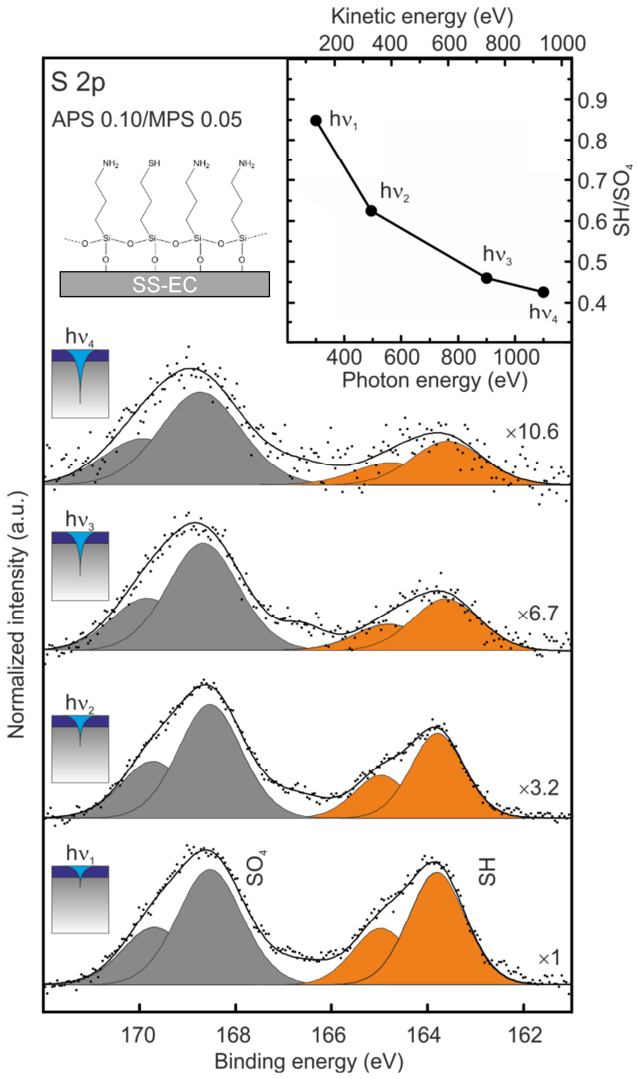

Figure 3.7. S 2p SR-PE spectra of APS 0.10/MPS 0.05 on SS-EC with different photon energies $h\nu_4$ = 1100 eV, (IMFP 26.00 Å), $h\nu_3$ = 900 eV (IMFP 21.55 Å), $h\nu_2$ = 494 eV (IMFP 11.90 Å), and $h\nu_1$ = 300 eV (IMFP 6.84 Å). SO_3 components at 167 eV are omitted for clarity. [Paper III]

The maximum depth of non-destructive depth profiling is $3\lambda cos\theta$ of the highest available photon energy. Non-destructive depth profiling does not yield quantitative results at a strictly defined depth, but it can be used to determine the average in-depth order of chemical bonds or elements. In this thesis, non-destructive depth profiling has been of utmost importance when determining the silane overlayer chemistry and in separating the substrate and adsorbate chemical groups.

3.3.4 Inelastic electron energy-loss background analysis

The thicknesses of the organic overlayers are typically determined by employing the Beer-Lambert equation (Eq. 3.3) or by employing other than electron spectroscopic methods such

as ellipsometry. The Eq. 3.3 is only valid for homogenous layers on homogenous substrates. Whereas it is safe to assume that the adsorbed organic molecules do not segregate into the substrate, it is not given that the adsorbed molecules will form homogenous, evenly thick surface monolayers or multilayers.

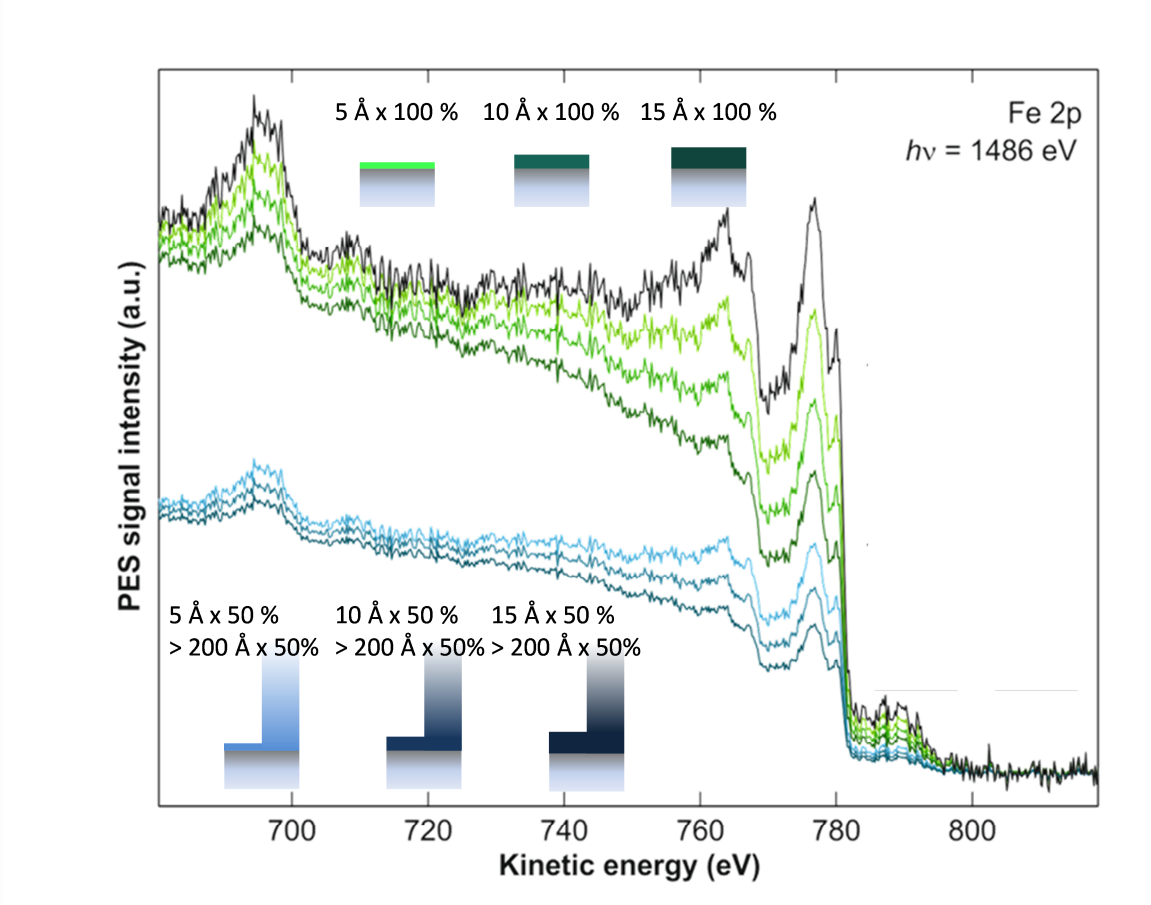

Figure 3.8. Measured Fe 2p XP spectrum of SS-EC (black). Modelled spectra of uniform monolayer (green) morphology and an island morphology (blue) where 50% of the surface is covered with silane clusters with the thickness of >200 Å thickness. Modified form the supplementary material of Paper IV.

For the adsorption of small atoms or molecules on a single crystal surface, a monolayer is traditionally defined as adsorbate coverage of one atom/molecule per one substrate atom. For TMA, the situation is more complex. In Paper I, it is shown that TMA adsorption geometries varying between flat-lying to upright (tilted) orientations depend on the TMA coverage and the molecule. In a flat-lying orientation, a TMA molecule covers approximately 13 Cu atoms [34] and in an upright position roughly eight atoms [93]. In the case of fully TMA covered Cu substrate, the coverage would yield values less than unity and different coverage values would be obtained for different molecular orientations. For self-assembly in general, a monolayer is defined as a densely packed layer of the adsorbate which fully covers the substrate surface. In

this thesis, the latter definition is used with TMA and Gly on Cu and silanes on steel. The coverages are determined by employing inelastic electron energy-loss background analysis (IEEB).

The IEEB offers information on the surface morphology. In the IEEB analysis, the inelastically scattered electrons with kinetic energies of 0-100 eV less than a photoemission peak of a given transition are analysed. The IEEB method has been developed by Tougaard [94– 96] and the required analysis procedures are included in the QUASES software [97]. The measured PES spectrum is described by

$$J(E_K, \Omega) = \int dE_0 F(E_0, \Omega) \int f(z) G\left(E_0, \frac{z}{cos\theta}; E_K\right) dz, \quad (3.7)$$

where F is the flux density of electrons excited from an atom to a solid angle Ω with initial kinetic energy E_0, $f(z)$ is the concentration of the atoms at the depth z, G is the electron energy distribution as a function of travelled path $z/cos\ \theta$, i.e. the probability that an electron with initial energy E_0 has an energy in the interval E, $E + dE$ after having travelled the path length $z/cos\ \theta$. The G depends on the total energy loss T of an electron moving through a solid. The energy loss depends on the inelastic electron scattering cross section $K(E,T)$ and the path travelled. In the determination of $K(E,T)$, Universal cross sections $A(T)$ are used.

$$\lambda(E)K(E,T) \cong A(T) = \frac{BT}{(C-T^2)^2+DT^2}, \quad (3.8)$$

where B, C and D are constants that have been determined for different classes of materials, such as metals, alloys, oxides and polymers [96].

The QUASES software yields a theoretical electron energy-loss background and a photoelectron peak based on the information on the surface morphology, the initial energy of emitted electrons, the inelastic electron mean free paths determined by the TPP-2M equation, ionization cross-section, the measurement geometry and the energy dependence of the spectrometer transmission function [94], [95]. In the analysis, the measured spectrum can be compared with the reference spectrum of known $f(z)$. By varying the surface morphology and composition of the model surface and by comparing the simulated result with the experimental result, the quantitative analysis of surface morphology and the composition of surface confined layers can be obtained.

This method has been established as a relevant method for the analysis of e.g. metal and alloy oxides [98– 101]. It has been used to a lesser extent with organic layers on metal and alloy surfaces. The IEEB has been used to determine organic overlayers with a few nanometre thickness [102–104]. In papers I and III and IV, the IEEB has been used to determine both surface morphology and thicknesses in the range of 0-40 Å thick organic overlayers.

Figure 3.8 shows a XP Fe 2p spectrum of SS-EC (black) as an active substrate (the attenuation of the substrate is studied) as a reference. Two surface morphologies with different thicknesses are presented with modelled spectra. Green lines show the modelled spectra of a uniform silane overlayer with a thickness of 5, 10 and 15 Å. As the uniform layer thickness increases, the inelastically scattered electrons are enhanced in comparison to the photoelectron peak at *KE* = 780 eV (*BE* = 706 eV). The blue lines represent island type surface morphology with relatively thick silane clusters (> 200 Å) and 5, 10 and 15 Å thick silane overlayers, both with equal coverage. Here, the modelled signal is further attenuated as the total amount of silanes is significantly increased with respect to the uniform morphology. The morphology differences are observed as differences in the slope of the inelastic electron energy background close to the photoelectron peak. The analysis depth of the method is up to 10λ and the depth resolution is λ/3. The error estimate for the method is ±15% [96].

3.3.5 Chemical derivatization

Chemical derivatization (CD) is a labelling and analysis method used with photoelectron spectroscopy. Labelling methods are used in other spectroscopy and analysis methods routinely. With PES, it is possible to determine the surface chemical groups, but intrinsically, PES does not provide information on the orientation of the surface chemical groups or their availability for forming bonds with other molecules. CD may be employed to recognize those functional groups at a surface that are available for binding with other molecules. Biofunctional properties of a surface often rely on the ability of the surface to bind biomolecules with a controlled distribution. Thus, it is important to determine not only a surface concentration, but the orientation of functional groups that provide binding sites for biomolecules.

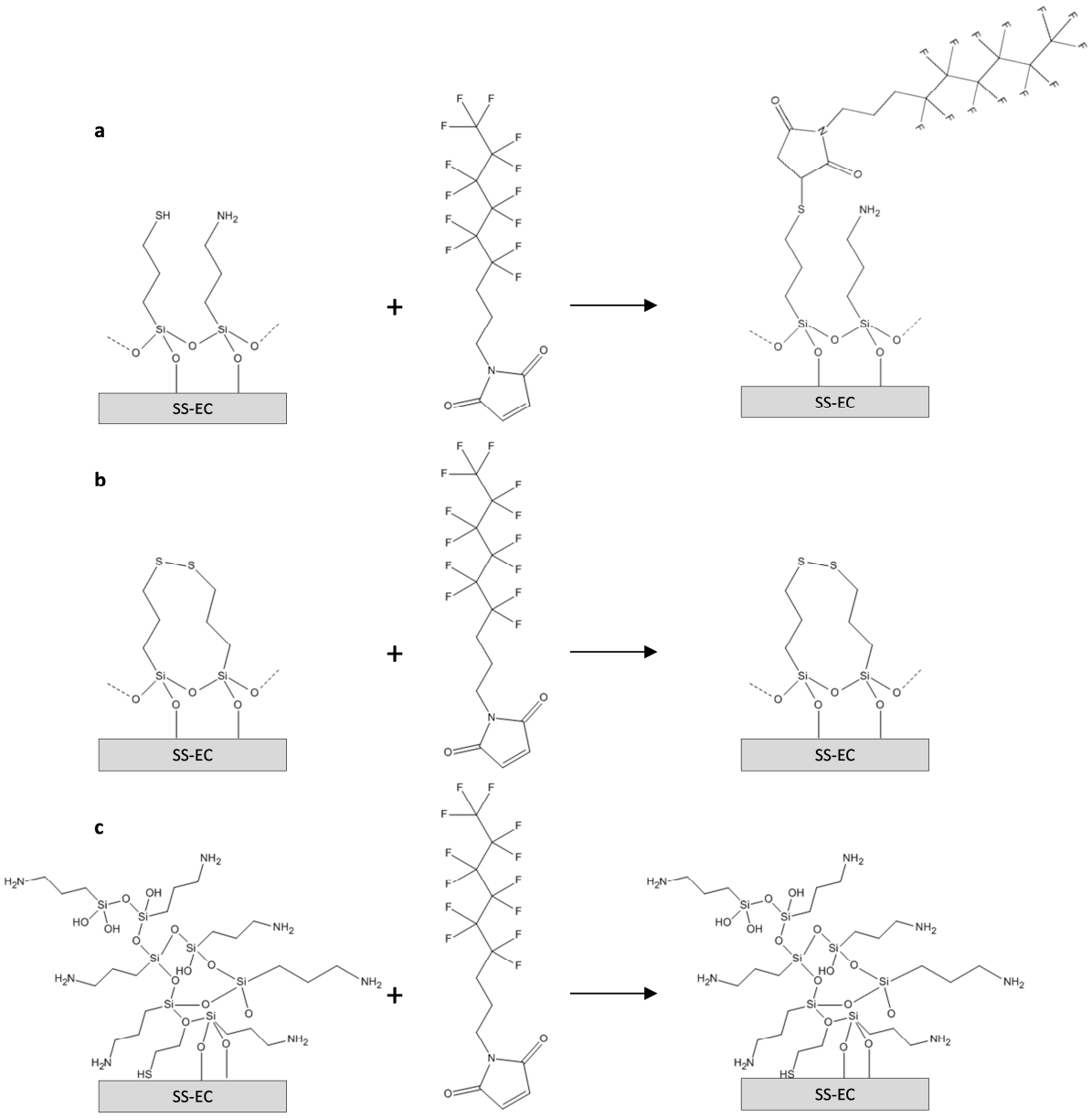

Figure 3.9. Schemes for MPS and MAL-F reactions (a) Maleimide terminus of MAL-F binds with SH-group of the MPS molecule. (b) If disulphide bonds are formed between neighbouring MPS molecules, MAL-F does not bind to the surface. (c) MAL-F does not bind to the surface because free thiols are not spatially available.

The label molecule contains an element which is not observed at the investigated surface and has a functional group which reacts with the surface functional group of interest. The sample is exposed to the label molecule either in the liquid or vapour phase. The liquid phase derivatization is straightforward and inexpensive, but the solvents may influence the surface, whereas the vapour phase derivatization reactions are difficult to implement, but yield more reliable quantitative results [105]. In this thesis, liquid phase CD was employed to determine the relative amount of thiols in MPS molecules that are available for binding in the APS

matrix at varied APS/MPS ratios. Liquid phase CD was chosen because the samples could be derivatized in a reproducible manner both at the MAX IV Laboratory and at the Surface Science Laboratory.

In this study, APS/MPS samples were labelled with *N*-(4,4,5,5,6,6,7,7,8,8,9,9,9-Trideca-fluorononyl)maleimide (MAL-F). Figure 3.9 shows schematically different outcomes of MAL-F exposure to APS/MPS surface. Maleimide is expected to bind with surface thiols under the experimental conditions (Figure 3.9 (a)). Adjacent thiol groups in the APS/MPS matrix at the surface may form disulphide bonds (S-S) during annealing and MAL-F bonding is inhibited (b). Disulphide and thiol are not resolvable in PE spectra, but the amount of disulphides can be estimated with CD. Tris(carboxyethyl) phosphine hydrochlorine solution (TCEP) reduces disulphides back to thiols. Thus, the differences in surface fluorine concentration in CD with and without TCEP treatment prior to MAL-F exposure can be used to estimate the S-S/SH ratio of APS/MPS surfaces. Figure 3.9 (c) represents a clustered APS/MPS surface, where the SH groups are not sterically available for MAL-F binding.

The CD was performed by exposing the sample to 0.5 mg/ml MAL-F in dimethyl sulfoxide (DMSO) for 60 min, followed by rinsing with DMSO, DI H_2O and drying with N_2. The TCEP treatment was performed by exposing the sample to 0.05 M TCEP for 15 min, followed by rinsing with DI H_2O and drying with N_2 prior to the MAL-F exposure. In the PES experiments of MAL-F labelled samples, the fluorine surface concentration was observed to decrease during exposure to irradiation. A probable reason for this is the cleavage of fluorine substituted carbon chains under irradiation. The small molecular weight fragments of such chains are easily desorbed. During the PES experiments of CD samples, F 1s and C 1s spectra were recorded both in the beginning and end of measurements of each sample, and sample exposure to the photon flux was avoided prior to data acquisition.

3.4 Scanning tunneling microscopy

Scanning tunneling microscopy (STM) is a surface analysis method, which enables the study of surface structures in atomic resolution. In this work, STM has been used to study the adsorption of Gly and TMA on Cu substrates. The operation principle of STM is shown in Figure 3.10. Briefly, a sharp tip (in this work made from tungsten wire [88]) is brought within the distance of a few nanometres of the sample surface. At this distance, when the sample and

the tip are biased, quantum mechanical tunneling occurs and a measurable current between the tip and the sample can be measured. When the tip is scanned across the sample an STM image is formed. In this thesis, constant current imaging (CCI) mode was employed. In CCI mode the current is maintained constant by a feedback loop controlled by a computer as the tip is moved across the surface in x,y and z directions by piezoelectric elements [106]. The produced STM image is a convolution of surface morphology and the electron density.

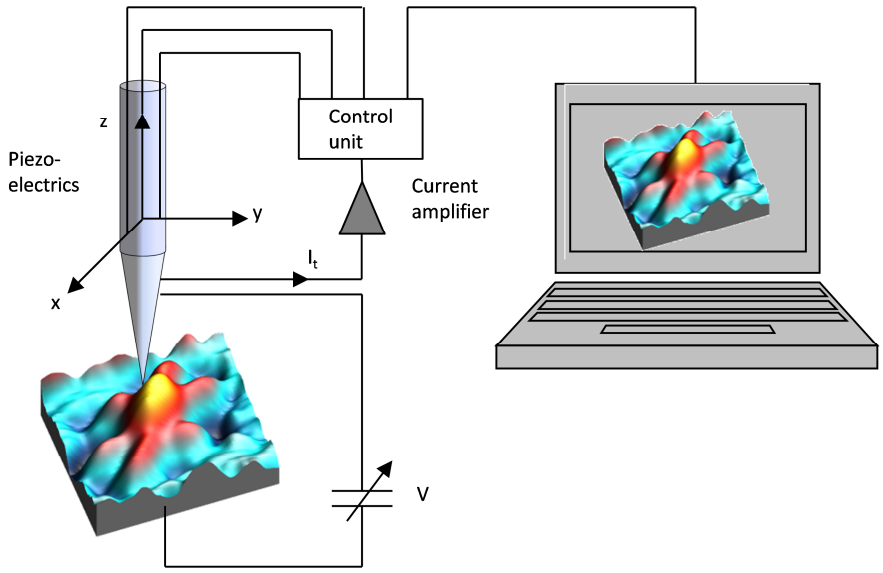

Figure 3.10. The operation principle of the scanning tunneling microscopy.

3.5 Density functional theory calculations

Density Functional Theory (DFT) is a computational method for calculating the electronic structure of matter. It is based on a quantum mechanical modelling and it uses functionals of electron density. Whereas many quantum mechanical calculation methods are based on the solving of the many-body Schrödinger equation, DTF uses electron density as a basic quantity. It can be used to calculate the geometric, electronic and spectroscopic properties of the studied systems [107]. In this work, DTF calculations were used along with STM images in the analysis of the surface phases of glycine on Cu(100)[Paper II].

4. MODIFICATION OF Cu AND STAINLESS STEEL SURFACES VIA SELF-ASSEMBLY OF ORGANIC MOLECULES

This chapter summarizes the key results presented in the papers of this thesis. Throughout this work, the underlying theme has been the study of the substrate-adsorbate and adsorbate-adsorbate interactions on organic-inorganic interface. Molecular level understanding of the surface phenomena are required for the controlled fabrication of nanomolecular organic layers on both single crystal and alloy oxide surfaces. Chapter 4.1 focuses on the adsorption behaviour of trimesic acid on Cu(100) with the main emphasis on the coverage dependency of the observed surface configurations [Paper I]. Chapter 4.2 highlights the chiral surface structures of achiral glycine on Cu(100) [Paper II]. In Chapter 4.3, the bifunctional overlayers of amino- and mercaptopropyl trimethoxysilanes on electrochemically treated stainless steel are scrutinized as a function of the liquid phase ratio of the silanes [Papers III and IV].

4.1 Effect of coverage on the TMA adsorption configuration and binding on Cu(100)

The properties of the TMA molecule, such as rigidity due to the benzene ring and three identical carboxyl end group,s facilitate a range of binding configurations on Cu(100) surface. As presented in Chapter 2.2.2, the carboxylic acids typically bind to a metal surface via a deprotonation of the carboxyl group to carboxylate ($COOH \rightarrow COO^- + H^+$). The TMA can bond in mono-, bi- or tridentate manner and thus adopt different molecular orientations from a flat-lying to an upright adsorption configuration at the surface.

The substrate properties of the Cu(100) also affect the TMA adsorption. Most prominently, the adatom and the step density are the key substrate properties that play a role in the adsorption phenomena. The coordination bonding is dependent on the adatom density and mobility, both of which can be controlled by the substrate temperature [Paper I]. Organic molecules often adsorb at the step edges in the initial stages of adsorption [Papers I and II and references therein]. The density of the steps, i.e. the terrace width, can be affected by the cutting of the single crystal and the annealing cycles performed on the sample. As the substrate temperature was constant for the TMA deposition, as well as for PES and STM

studies, and all the experiments were performed on the same single crystal Cu(100), the substrate properties are considered constant and are not discussed further.

4.1.1 Coverage induced changes in the molecular orientation of TMA on Cu(100) observed in the PES analysis

Figure 4.1 exhibits the C 1s XP spectra of TMA/Cu(100) samples with increasing surface coverage from the bottom to the top. The TMA coverages (θ_{TMA}) were calculated from the IEEB results as $\theta_{TMA} = \gamma d$, where d is the TMA adlayer height and γ is the fraction of substrate area covered with the adlayer.

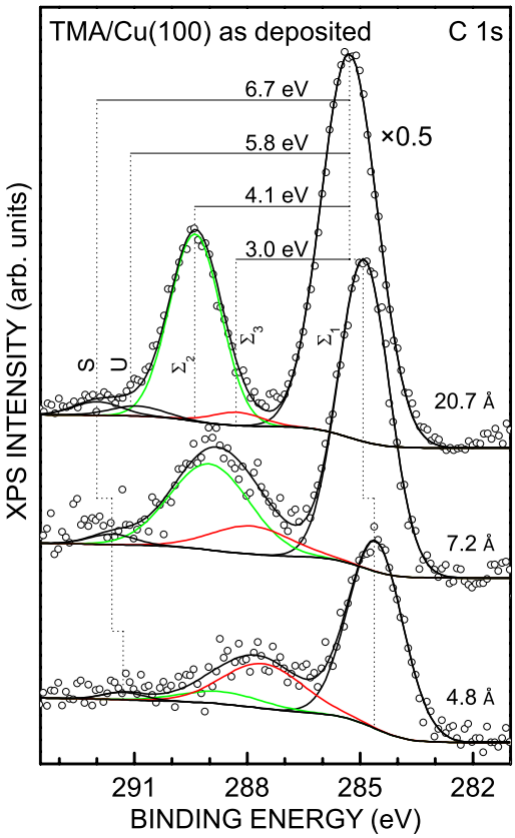

Figure 4.1. C 1s XP spectra of TMA/Cu(100) measured after different depositions, hν = 1253.7 eV. The intensity of the topmost spectra is multiplied by 0.5. [Paper I]

The C 1s XP spectra exhibit four components on all samples. The components at the lowest and highest binding energies originate from the phenyl ring of the TMA molecule. The large peak at low *BE* (Σ_1) is the main peak and the small peak at +6.7 eV in respect to the main peak is the shake-up satellite (S) of the aromatic ring. The peaks inbetween, at +4.1 eV and

+3.0 eV distance from the main peak are attributed to carboxyl (Σ_2) and carboxylate (Σ_3), respectively. Angle resolved XPS measurements verify that the surface bonding via deprotonation occurs as presented in Equation 2.1. The relative amount of COO^- bonds increases as the sampling depth doubles, while the COOH signal behaves oppositely, indicating that the COO^- signal originates from the Cu-TMA interphase and the COOH from the outmost surface.

A closer look at Figure 4.1 reveals two TMA coverage dependent phenomena. Firstly, the relative intensity of COO^- in respect to COOH intensity changes at different coverages, indicating coverage dependent changes in the degree of deprotonation and thus coverage dependent surface orientation. Secondly, the main peak shifts towards larger binding energies with increasing coverage.

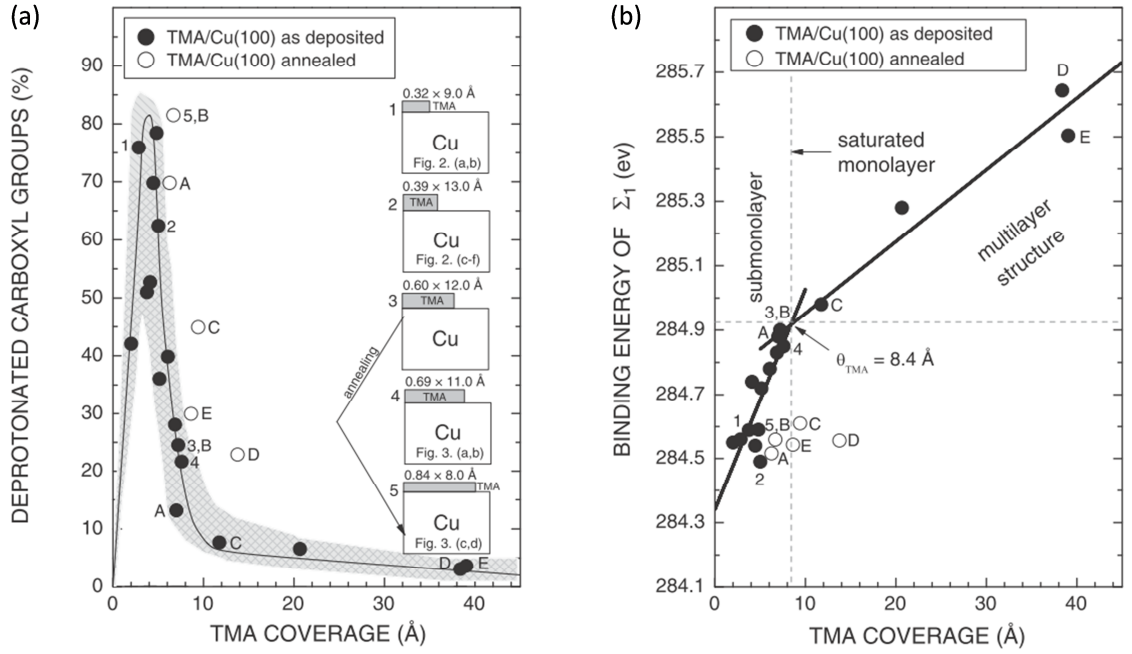

Figure 4.2. (a) Degree of deprotonation of TMA molecules as a function of coverage for the depositions at room temperature and after the subsequent annealing. (b) Binding energy of the phenyl component (Σ_1) vs. the TMA coverage for the TMA depositions at room temperature and after the annealing. A break in the slope corresponds to a saturated monolayer (8.4 Å). Letters A–E denote TMA depositions before (filled dots) and after (open dots) annealing. Modified from Paper I.

Figure 4.2 (a) shows an interesting behaviour of deprotonated carboxyl groups as a function of the TMA coverage. XPS provides averaged information from a relatively large area (in this case, the diameter of the sampled area is 600 μm). At submonolayer coverages, the adsorption configurations do not necessarily have a long-range order and many surface phases coexist at

the surface. The degree of deprotonation rises rapidly at low TMA coverages until a maximum at 80% is reached at 4-5 Å TMA coverage. As the coverage increases, the deprotonation degree falls rapidly below 10%, after which the deprotonation degree approaches 0%. This shows that the TMA molecules adopt different configurations at different TMA coverages. The initial rise of the degree of deprotonation indicates transformation from physisorbed TMA to mostly flat-lying, fully protonated TMA at the maximum of the deprotonation curve. The rapid decrease of the degree of deprotonation at coverages > 5 Å can be attributed to change from the flat-lying orientation to the upright one. As the coverage increases, eventually all the intensity originates from physisorbed TMA adlayer (sampling depths for C 1s, O 1s and Cu 2p are 40.7 Å, 52.6 Å and 18.3 Å, respectively) and the TMA/Cu interface is not detected.

In Figure 4.2 (b), the coverage dependency of the C 1s binding energy is illustrated. The figure shows that the *BE* of the phenyl ring peak is linearly dependent on the coverage with a clear change in the slope at 8.4 Å, which agrees with the geometrical size of the TMA molecule (8 Å) [31]. At 8.4 Å, the Cu surface is covered with a saturated monolayer, and as the coverage increases, the 2D growth mode changes into 3D growth with no ordering.

The changes in the phenyl *BE* can be attributed to at least two phenomena. Firstly, the *BE* shifts reflect the molecular orientation and hence the packing density. Coulombic interactions between the C 1s core-hole and the valence electrons in the Cu(100) conduction band lower the binding energy. The Coulombic force is inversely proportional to r^2, where the r is the distance between the core hole and the valence electron. Thus, the *BE* is smaller for C atoms in flat-lying TMA with all the carbon atoms close to the Cu surface compared with C atoms in upright oriented TMA molecules. Similar behaviour has been reported for alkanethiol SAMs on Au [108] and for carboxylic acids on Cu(100) [109]. Secondly, it has also been reported that the C 1s *BE* of organic molecules on metal substrates is higher by a few eV on multilayer samples than on monolayers if the molecules are chemisorbed in the monolayer [110]. If the molecules are physisorbed at the metal surface, the *BE* difference is negligible. This is attributed to the initial and final stage effects of the photoionization process. Physisorbed molecules are expected to undergo relaxation only after ionization (a final stage effect), whereas the chemisorbed molecules may also exhibit lower *BE* due to overlapping molecular orbitals and metallic band (an initial stage effect) [110]. Thus, chemisorbed molecular structures would exhibit lower *BE* than physisorbed. Also, at high TMA adlayer coverages,

charging effects during XPS measurements may increase the *BE* as the Cu electrons cannot compensate for the ionization of TMA.

On both Figure 4.2 (a) and (b), the annealed samples are presented in open circles. On all samples, upon annealing the TMA coverage and C 1s *BE* decrease, as the degree of deprotonation increases. The decrease in the coverage is attributed to desorption of physisorbed TMA. The changes in the C 1s *BE* and the degree of deprotonation suggest flat-lying orientation of TMA on annealed samples.

4.1.2 Adsorption stages of TMA on Cu(100) as observed by STM

STM studies of the TMA/Cu(100) reveal five distinct coverage dependent adsorption stages as a function of the TMA coverage and post-annealing. These stages are illustrated in Figure 4.3.

Stage I: At this stage, the overall coverage of TMA is small and no long-range order is observed. In large scale images (shown in Paper I, Figure 2(c)), signal noise at terraces is interpreted as mobile 2D Cu adatoms [93], [111], [112] and TMA. Local hexagonal TMA rings with Cu aggregates of several atoms trapped inside at step edges are observed. The immobile TMA molecules are flat-lying. The degree of deprotonation at ~75% arises from the combination of fully deprotonated (100%) TMA in hexagonal arrangements and mobile TMA (0%).

Stage II: As the TMA coverage increases, long-range ordering is observed. The TMA molecules adopt a cloverleaf structure (TMA_4Cu) with a long-range order, but not saturated monolayer coverage. The Cu adatoms coordinate four TMA molecules ($Cu(TMA)_4$), and, also, some $Cu_2(TMA)_6$ arrangements are observed. The deprotonation degree is ~63%. The deprotonation is lower than expected (100%) due to coexisting physisorbed mobile TMA in addition to the cloverleaf structure.

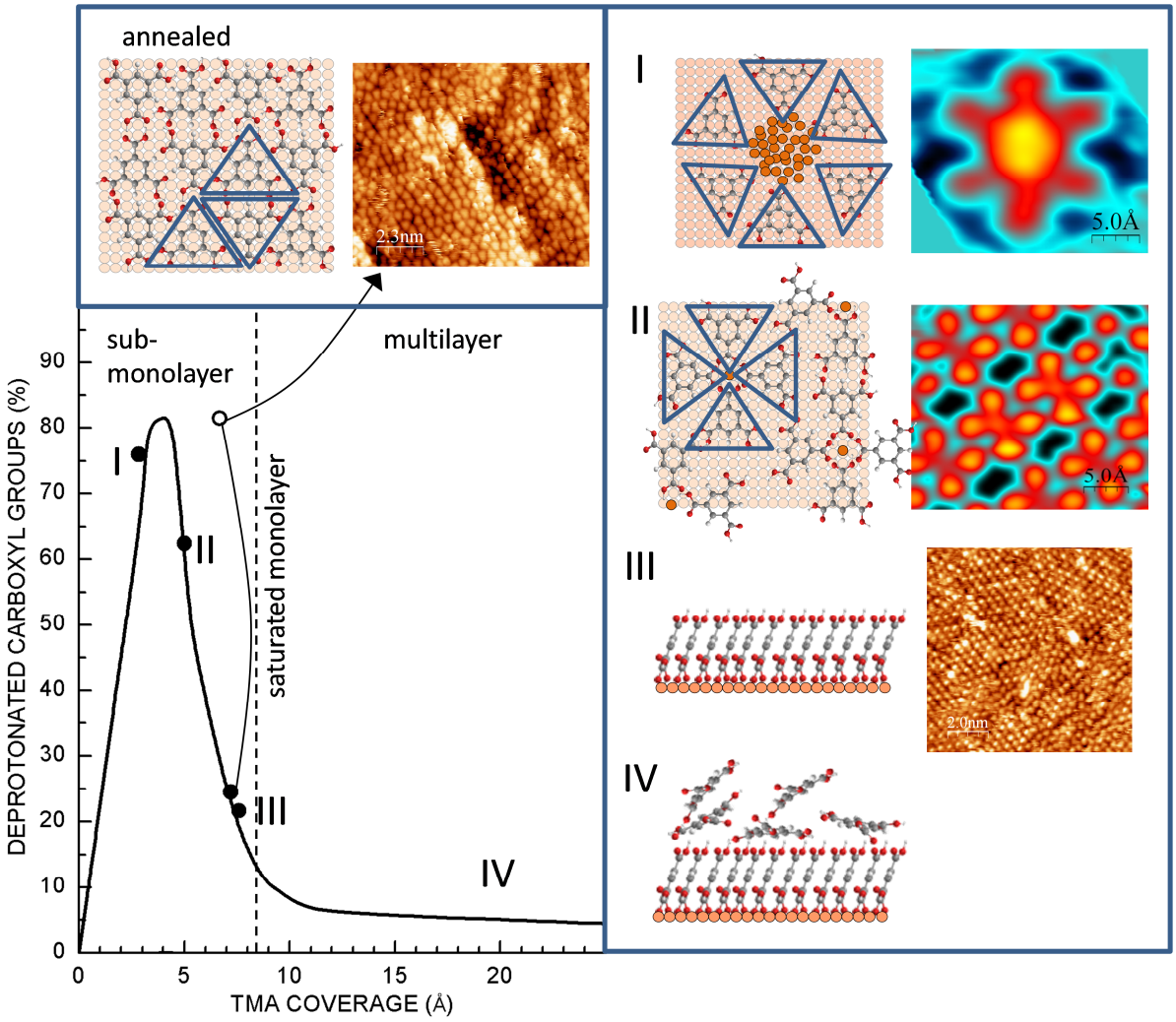

Figure 4.3. Five coverage dependent stages (I-V) of TMA adsorption on Cu(100) illustrated as STM images, schematic presentations (not to scale). The STM images are from Paper I.

Stage III: At this stage, the TMA coverage has increased further and a saturated monolayer is formed at θ_{TMA} = 8.4 Å. The increasing packing density leads to upright or tilted orientation. In this configuration, the TMA molecules form bonds with Cu atoms at terraces instead of adatoms. In the STM images, a chain structure is observed. The degree of deprotonation for the chain structure is 41.7%, due to COO^-:COOH ratio of 5:7 [93]. The degree of deprotonation has dropped to 20%. This suggests that the chain structure coexists with local multilayer or 2D gas phase.

Stage IV: As the coverage exceeds the saturated monolayer, the bonding mechanisms change. The adsorbed TMA molecules do not interact with Cu(100) and are physisorbed on a densely packed TMA monolayer. Hydrogen bonds may exist between the TMA molecules, but neither covalent bonding nor ordered structures exist.

Stage V: A fifth adsorption stage is achieved with annealing. A densely packed surface configuration with flat-lying TMA is shown in the STM image in Figure 4.3. Similar observations have been reported by Dmitriev et al. [93].

4.2 Chiral adsorption structures of glycine on Cu(100)

In this chapter, the adsorption behaviour of Gly on Cu(100) is discussed. The PES analysis and comparison with TMA/Cu(100) is presented in Chapter 4.2.1. Glycine adsorption configurations observed in STM images are summarized in Chapter 4.2.2.

4.2.1 Comparison of Gly and TMA adsorption on Cu(100) observed by PES

Figure 4.4 depicts the C 1s SR-PE spectra of as-deposited and annealed Gly/Cu(100) samples. The spectra feature four distinct components, which can be assigned to the carbon atoms in the glycine molecule, C–N (Σ_2, 286.0 eV), COO^- (Σ_3, 288.0 eV) and COOH (Σ_4, 289.8 eV) and to C–C bonds at the lowest binding energy (Σ_1, 284.5 eV). The C 1s spectra do not rule out any of the adsorption configurations presented in Figure 2.3. The presence of COOH indicates either small amount physisorbed glycine or bonding only via amino terminus (Figure 2.3 (f)). The surface concentration of COOH is low on all samples. The origin of C–C component is not clear. According to stoichiometric analysis, the molecules stay intact upon adsorption so the small component can be attributed to C–C impurities from the glycine powder.

Bonding via amino and carboxyl termini (Figure 2.3 (g)) is reported to be the dominant bonding arrangement on Cu(100) at room temperature [37–39]. The bonding via the amino terminus of the Gly molecule is not directly observed in the N 1s, or Cu 2p spectra. AR-XPS reveals, though, that when the surface sensitivity is increased, the COO^- and C–N intensities increase in the same ratio (both increase by 2.5 -fold), suggesting equidistance of these bonds from the Cu surface, which favours bonding via carboxyl and amino termini (Figure 2.3 (g)) over upstanding arrangements, as depicted in Figure 2.3 (e) and (f). The N 1s spectra (data not shown) show a single component at 399.6 eV, which indicates that the NH_2 is either in a neutral state or bonds with Cu.

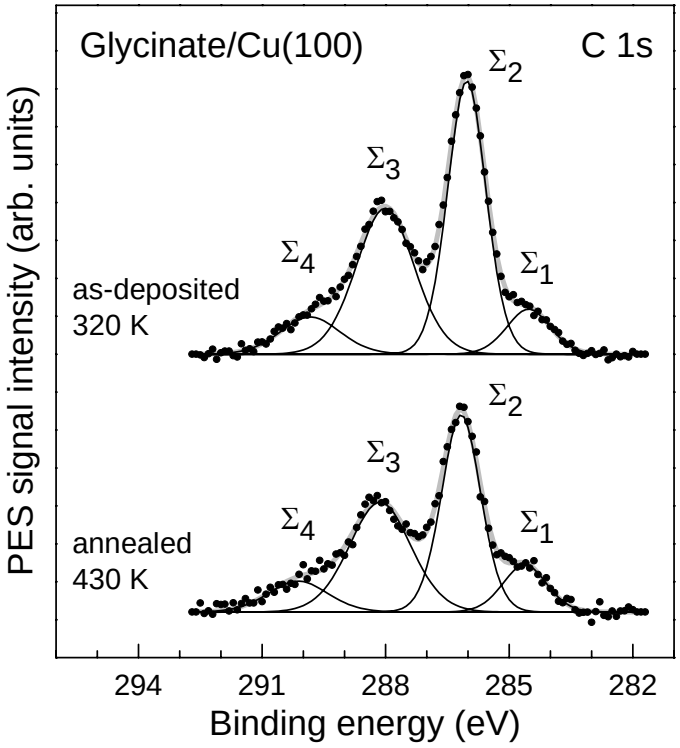

Figure 4.4. C 1s SR-PE spectra revealing chemical bonds on glycine/glycinate covered Cu(100), hν = 700 eV. [Supplementary material of Paper II].

The O 1s spectra of Gly/Cu(100) samples typically exhibit a narrow peak, which indicates that the surface oxygen adopt a well-defined single state. This supports adsorption configuration with both oxygen atoms of the carboxyl group bonding with the Cu substrate (Figure 2.3 (e) and (g)). Annealing is shown to decrease the amount of adsorbed glycine and increase the degree of deprotonation, as was observed on TMA/Cu(100).

The degree of deprotonation is significantly high on all Gly/Cu(100) samples (79% in Figure 4.4) and does not show Gly coverage dependent changes at submonolayer coverages. Coverage dependent changes in the C 1s *BE* are not observed to the same extent that on TMA/Cu(100) samples. Both of these observations elaborate the adsorbate dependent variations on adsorption configurations. Whereas TMA is rigid and has three symmetrical COOH groups, the glycine is more flexible. Thus, the increase in the coverage leads to changes in the degree of deprotonation and thus the molecular orientation in TMA/Cu, but PES analysis does not show coverage significant changes in the surface chemistry of Gly/Cu. Hence, the PES analysis supports the general consensus of tridentate adsorption configuration of Gly/Cu(100) at room temperature, although minor amounts of glycine may be also physisorbed at the surface.

4.2.2 Homo- and heterochiral surface domains of glycine on Cu(100)

The STM images of Gly/Cu(100) typically show triangle protrusions (see Figure 4.5), which are interpreted as tridentate glycinate bonding. Although tridentate glycinate molecules are chemically equivalent, they may adsorb on Cu(100) in several non-equivalent surface phases in terms of the binding sites of each surface covalent bonds and their spatial arrangement in respect of each other. In fact, the observed Gly/Cu phases are different in terms of chirality and they exhibit structural and electronic anisotropy [Paper II] and hence different types of functionality.

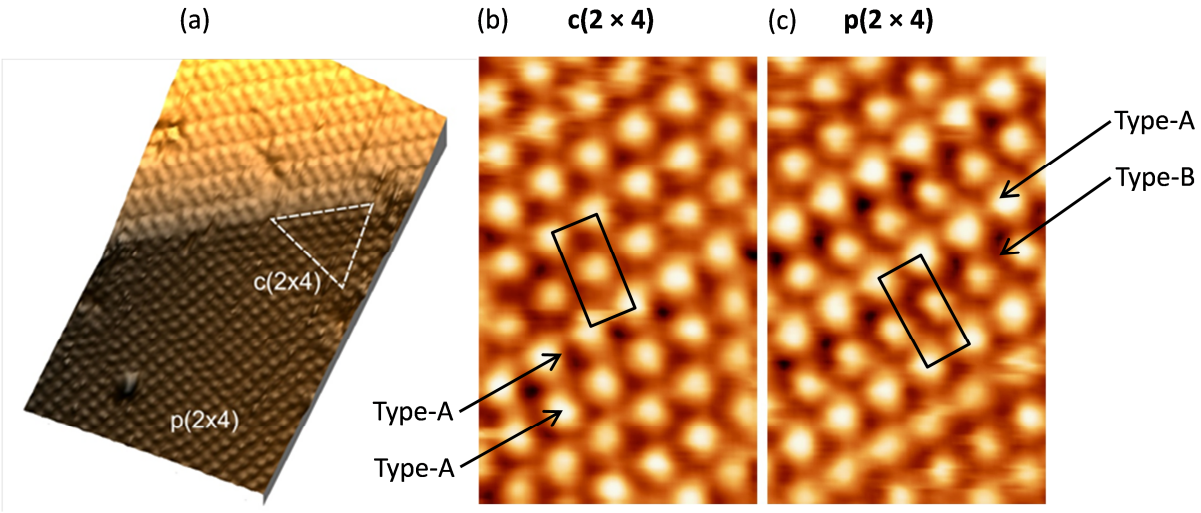

Figure 4.5. 3D STM image of the Gly/Cu(100) surface (18.8 nm × 11.0 nm) with coexisting c(2 × 4) and p(2 × 4) phases (a). High resolution STM images (3.0 nm × 4.8 nm) of (b) c(2 × 4) and (c) p(2 × 4) phases. The unit cells and Type-A and Type-B molecules are indicated. Modified from Paper II.

In Figure 4.5 (a), both c(2 × 4) and p(2 × 4) glycine domains are observed on Cu(100). The domains are at the lower terrace of <310> step edges. The <310> step formation is Gly adsorption induced, as these steps never appear on bare Cu(100) [37], and is an example of adsorbate induced substrate faceting. The Gly protrusions in the c(2 × 4) phase (Figure 4.5 (b)) are of equal intensity and, hence, occupy identical adsorption sites (Type A). The c(2 × 4) domains are homochiral (the molecules are superimposable on each other).

The p(2 × 4) domains are observed next to triangular c(2 × 4) domains [37]. The STM image of p(2 × 4) domain (Figure 4.5 (c)) shows triangular protrusions that, again, are consistent with tridentate bonding. In addition to different unit cell structure, the protrusions in

alternating rows show different brightness, which is an indication of different binding configurations (Type-A and Type-B). The p(2 × 4) domains are heterochiral (the Type-A and Type-B protrusions are not superimposable),although both glycine and Cu(100) are achiral.

Different structural models have been proposed to gain insights into glycinate surface configurations both with experimental and theoretical methods [37– 40, 113, 114, Paper II]. The Paper II introduces a new DFT based structural model for p(2 × 4) domain, which is in agreement with the STM images. The model proposes that the observed brightness differences in p(2 × 4) are due to different oxygen atom binding sites at different heights on Cu(100) (see Figure 2.2 (a).

4.3 Bifunctional APS/MPS monolayers on stainless steel

APS/MPS overlayers were prepared on SS-EC with the aim to incorporate MPS molecules in APS matrix with a controllable MPS spatial distribution, high packing density and upright oriented silane molecules. With the employed fabrication parameters, APS forms a monolayer with a 0.10 v-% solution concentration [56]. Initial observations of the adsorption of MPS and the coadsorption of APS and MPS showed two interesting phenomena. Firstly, under the same fabrication parameters that lead to a monolayer formation of APS, MPS is sparsely adsorbed with no long-range ordering. Secondly, in the coadsorption of APS and MPS, the APS/MPS ratio at the surface differs from the same ratio in the solution. Hence, an extensive set of samples with a constant APS concentration of 0.10 v-% and a varied concentration of 0.01-1.00 v-% of MPS were fabricated.

4.3.1 Surface morphology of APS/MPS on SS-EC

Figure 4.6 introduces the IEEB analysis of two APS/MPS samples. The Fe 2p XP spectrum of the SS-EC sample was used as a reference and the attenuation of the Fe 2p signal on silanized samples was used to determine the silane overlayer thickness and surface morphology.

On all APS/MPS samples, the IEEB analysis yielded a surface morphology of a thin overlayer (6.6-16.8 Å) and a thick (> 200 Å) island. The surface morphologies are schematically

illustrated in Figure 4.6 (a), and the thin overlayer thickness in addition to coverage are plotted as a function of MPS solution concentration in Fig 4.6 (b). The IEEB analysis shows that the surface area is completely covered with a silane overlayer. This is significant as the silane overlayers may enhance corrosion protection and act as a barrier layer against water if the overlayers cover the substrate surface uniformly, whereas uncovered areas in the silane overlayer may induce local corrosion. The thin overlayer thickness varies slightly as a function of the MPS solution concentration, mostly within reported thicknesses between 5-11 Å [19, 55, 56, 65] for APS and MPS monolayers.

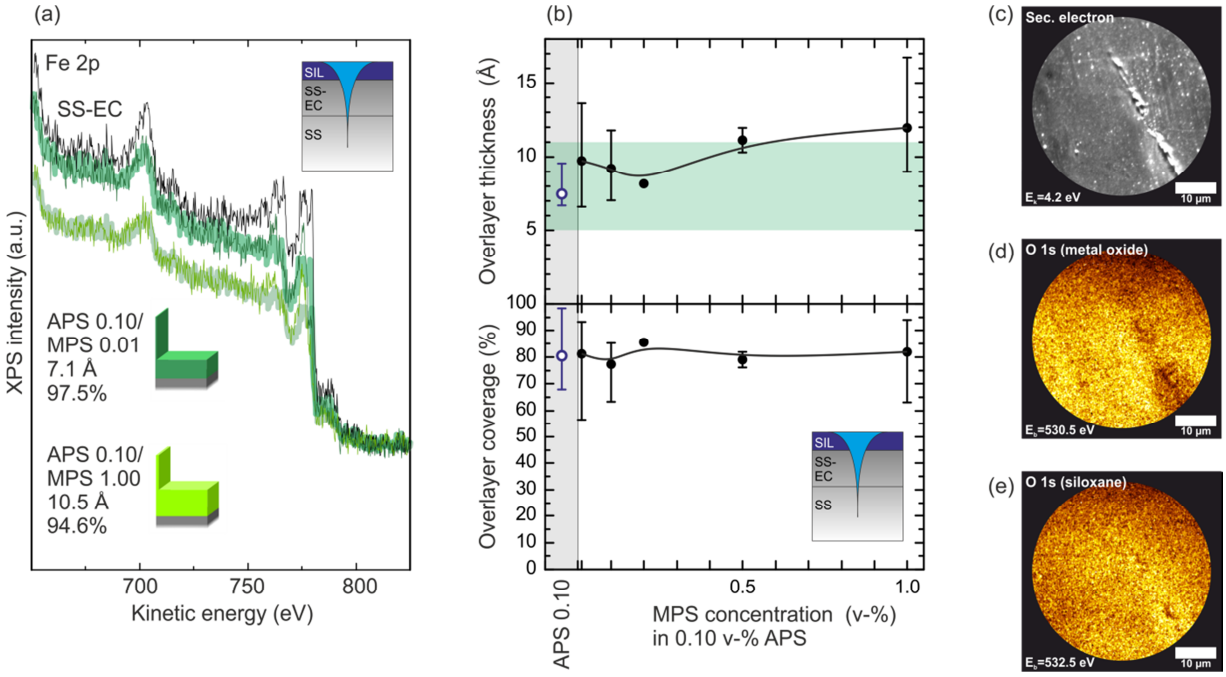

Figure 4.6 (a) IEEB analysis of Fe 2p region ($h\nu$ = 1486.6 eV) of the reference sample SS-EC (black) and APS 0.10/MPS 0.01(dark green) and APS 0.10/MPS 1.00 (light green). The best fit between experimental (thin lines) and modelled (thick line) data is achieved with the surface morphologies shown in the schematic illustrations. The bars represent highly clustered islands with thickness > 200 Å. (b) Thickness (top) and coverage (bottom) of the thin silane overlayer as a function of the MPS solution concentration. The green area depicts literature values for the monolayer thickness of APS and MPS. The data points represent the average value and the vertical lines define the range of variation. The lines are to guide the eye only. Spectromicroscopy images of APS 0.10/MPS 0.01 sample: (c) Secondary electron image (Hg lamp, $h\nu$ = 5.2 eV), EF-XPEEM images ($h\nu$ = 1486.6 eV) of O 1s (d) metal oxide and (e) siloxane. [Paper III]

Two types of deviations from ideal monolayer bonding are observed in the IEEB results. Firstly, the slight increase in the thin overlayer thickness at higher solution concentrations of MPS indicates that the overlayer thickness exceeds a monolayer thickness. This observation suggests that with high MPS solution concentrations the ordering is hindered by MPS. Secondly, the unexpectedly thick islands were observed on all APS/MPS samples. Spectromicroscopy study of APS 0.10/MPS 0.01 samples shed light into the origin of these

thick > 200 Å islands. Figure 4.6 (c) illustrates a secondary electron image of the sample. The image shows a relative smooth surface area with a protrusion across the imaged area. The EF-XPEEM images of the same area reveal that the siloxane bonds at 532.4 eV are in abundance on and around the protrusion, whereas the metal oxide signal at 530.0 eV in the same region is attenuated. This suggests that silane clusters are trapped around surface irregularities in the sample fabrication process. This is in good agreement with observed thick islands (>200 Å) in the IEEB analysis.

4.3.2 Coadsorption of APS and MPS on stainless steel

Figure 4.7 (a) and (b) show the relative surface concentrations (calculated as percentages of the elements in silanes; C, O, Si, N and S) of the components observed in N 1s and S 2p XP spectra as a function of the MPS solution concentration. The NH_2, NHC=O and NH_3^+ originate from the APS molecules. The NHC=O denotes carbamates which are formed when the amino groups react with atmospheric CO_2 [42]. The NH_3^+ are deprotonated amino groups that often bind to the substrate via surface OH–NH_3 interaction (see Figure 2.4) [42, 64].

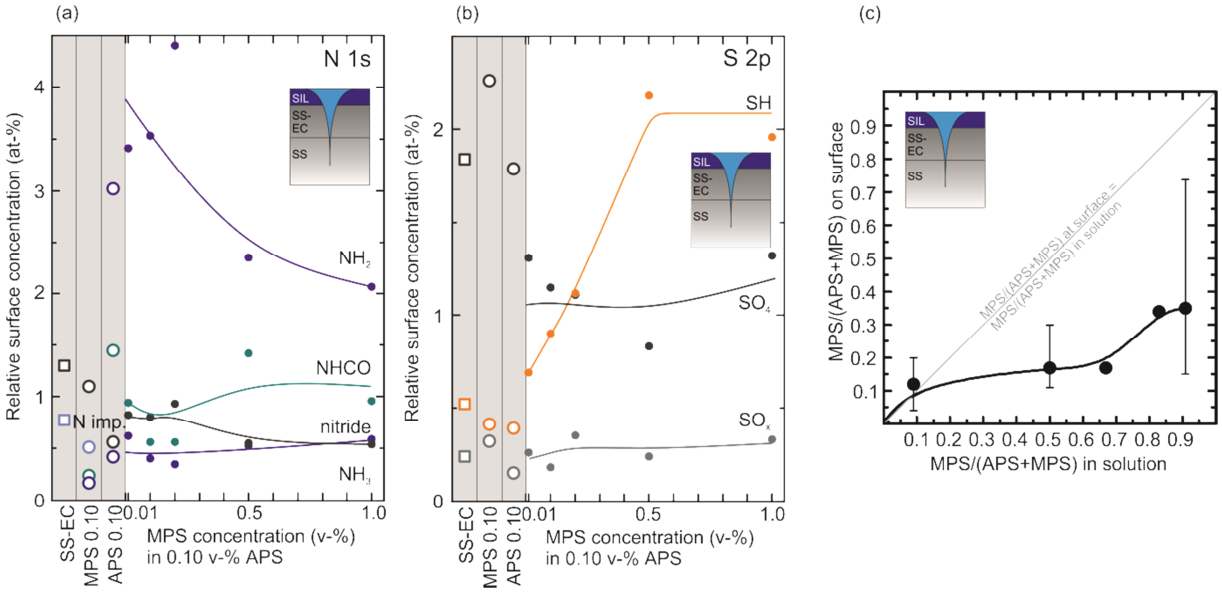

Figure 4.7. Relative surface concentrations of the chemical states of (a) nitrogen and (b) sulphur of the references and APS/MPS samples as a function of the MPS solution concentration in 0.1 v-% APS (hν = 1486.6 eV). Data points represent average values of a set of experiments performed on several individually prepared samples for each APS/MPS ratio. Lines are to guide the eye only. (c) MPS/(APS+MPS) ratio at the surface as a function of MPS/(APS+MPS) ratio in solution. Data points represent the average value and the vertical lines define the range of variation. Modified from Paper III.

In Figure 4.7 (a) and (b), a simultaneous decrease in the NH_2 signal, as the amount of SH increases along with increasing MPS solution concentration, shows that the relative amount of MPS in the APS/MPS overlayer increases and APS decreases. This is also shown in Figure 4.8 (c) where the surface and solution concentrations are plotted. The MPS surface concentration shows a non-linear dependency on the solution concentration. Except for very small solution concentrations, the surface concentration is significantly smaller than the solution concentration.

Figure 4.7 (b) also shows that the amount of MPS (SH) on all samples with both APS and MPS is clearly higher than on MPS 0.10. This shows the synergetic effect of coadsorption of APS and MPS. In the fabrication process, the hydrolysis solution pH was not adjusted. The native pH of MPS in the hydrolysis solution is 7. At this pH, the hydrolysis of MPS is very slow [10]. The decrease or increase of pH by one unit includes a ten-fold increase in the hydrolysis rate [10]. The native pH of APS under the same conditions, on the other hand, is 10.6. Thus, in the presence of APS, the pH of the hydrolysis solution is basic and increases the hydrolysis rate, which leads to higher amount of adsorbed MPS. Still, the amount of unhydrolyzed silanes at the surface increases as the amount of MPS increases. This is determined from the surface concentrations of C–O [Paper III, 11, 45].

The relative surface concentration of MPS saturates around 30%. This is due to short hydrolysis and silanization times employed in this study. It has been shown that with constant total amount of silanes and variable APS/MPS ratio in solution, the surface concentration of MPS may exceed the solution concentration with longer silanization times [72]. In both cases, the surface concentration of the APS and MPS cannot be determined from the solution concentration.

4.3.3 Non-destructive depth profiling of APS/MPS samples

All the elements in the silanes are also present in the SS-EC substrate. In Figure 3.7 it was shown that the SH bonds originate from the topmost surface of APS 0.10/MPS 0.05 and the SO_4 is buried in the SS-EC. This shows that the MPS molecules are oriented in an upright manner at low MPS solution concentrations. In the case of the sulphur concentrations in the substrate and the organic overlayer, the determination of origin of the signal with different photon energies was straightforward, as the SO_4 and SH binding energies are sufficiently

apart as shown in Figure 3.7. For the other elements in the silane, the situation is more complex because the components often overlap. In Paper III, the observed chemical states and their in-depth origin are discussed in detail.

Figure 4.8 (a) shows the O 1s SR-PE spectra of APS 0.10/MPS 0.01 (SIL1) and APS 0.10/MPS1.00 (SIL2) probed with a surface sensitive photon energy of 720 eV. The peak at the lowest *BE* (M–O, 530.0 eV) incorporates all metal oxides, mainly Fe_xO_y and Cr_xO_y in the SS-EC substrate [56]. The peak at 531.4 eV is attributed to OH groups at the surface [19] and the peak at 532.4 eV to siloxane bonds (Si–O) [19, 63] and SO_4 residue in the SS-EC [56]. The small peak at the highest binding energy is from C=O impurities [63]. The relative amount of siloxane bonds is higher on SIL2 than on SIL1. This indicates a higher silane overlayer thickness on SIL2. This is also consistent with a more attenuated M–O signal on SIL2. It is noteworthy that the OH component is observed on both samples. This shows that the surface hydroxylation with EC treatment is sufficient, as only part of the surface OH are consumed in the silanization and annealing process.

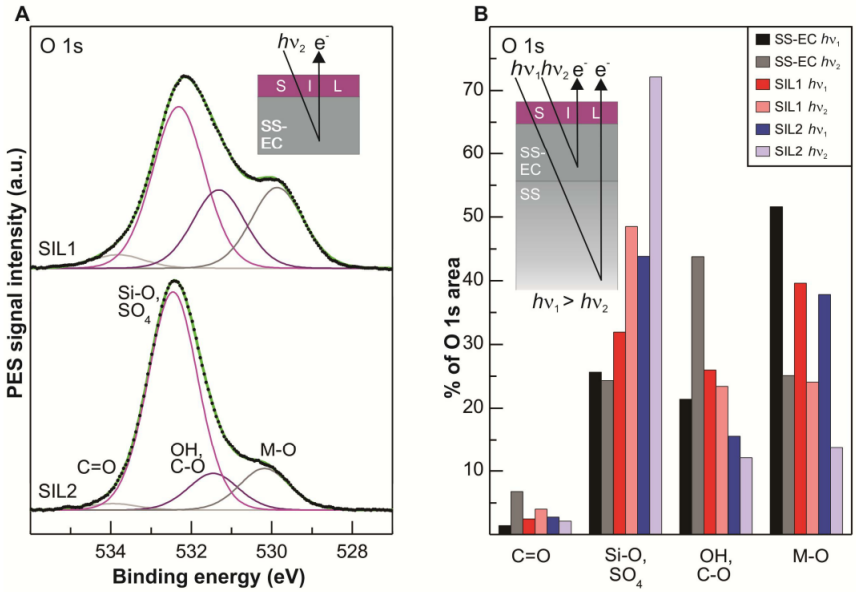

Figure 4.8. SR-PES results of O 1s spectra and IEEB analysis. (A) The O 1s SR-PE spectra of samples SIL1 (APS 0.10/MPS 0.01, top) and SIL2 (APS 0.10/MPS 1.00, bottom). The schematic illustration demonstrates the sampling depth of emitted electrons in SR-PES experiments with photon energy $h\nu_2$ of 720 eV. (B) The different components in O 1s spectra for SS-EC, SIL1 and SIL2 are shown in percentages of total O 1s signal. The inset demonstrates the difference between sampling depths for the two photon energies ($h\nu_1$ =1486.6 eV and $h\nu_2$ = 720 eV). [Paper IV]

Figure 4.8 (b) shows the results of non-destructive depth profiling of the O 1s SR-PE spectra of the abovementioned silanized samples and the SS-EC substrate. The samples were probed

with two photon energies (1486 eV and 720 eV). The results show that the SO_4 is distributed throughout the SS-EC oxide layer as the relative concentration of SO_4 does not change when the sample is probed different photon energies. On the other hand, it is clear that the OH is confined to the topmost surface layers of SS-EC. The increase in the SO_4/Si–O signal upon silanization shows that silane molecules are adsorbed on the SS-EC (this is naturally also observed as an increase in the Si intensity).

Table 4.1. The chemical states observed in the SR-PES analysis and their origin determined by non-destructive depth profiling. The grey background indicates in which regions (APS/MPS overlayer, SS-EC or SS) the elements are observed. The in-depth origin of the chemical states is indicated in the columns (e.g. NH_3^+ is observed at SS-EC/silane interface and NH_2 in the outermost region of the silane layer. M denotes all the metals in the SS substrate. The information is collected from papers III and IV and from [72].

	C	**O**	**Si**	**N**	**S**	**M**
APS/MPS overlayer	C–N C–C C–O, C=O	Si–O	Si–O	NH_2, NHC=O NH_3^+	SH S–M	
SS-EC	C=O	M–O, SO_4, OH	SiO_2	N impurities	SO_4, SO_x	M–O
SS	C		Si	nitrides	sulphides	M

Similarly, the in-depth origin of other surface chemical states can be determined with non-destructive depth profiling. The chemical states observed in the SR-PES analysis and their in-depth origin are listed in Table 4.1.

The orientation of the APS was determined from the C 1s SR-PE spectra. It was observed that the C–N bonds are located closer to the sample surface than C–C bonds, which in turn are above C–O and C=O bonds [72]. The only source of C–N bonds on the samples is the bond between the spacer backbone and organofunctional group of APS. The C–C bonds originate from the spacer backbone and adventitious carbon, whereas C–O bonds are both impurities and unhydrolyzed methoxy groups in silanes. This shows that also the APS molecules oriented mostly in an upright manner. Some APS molecules are oriented upside down, which is observed as NH_3^+ at the silane SS-EC interface. The surface concentration of NH_3^+ increases slightly as the solution concentration of MPS increases suggesting that the incompletely hydrolysed MPS inhibits the upright orientation of APS.

4.3.4. Determination of the surface functionality with chemical derivatization

Although the non-destructive depth analysis indicates that the organofunctional groups are mostly oriented outwards of the surface, the functionality i.e. the availability of the thiol

groups for bonding with other molecules cannot be determined by photoelectron spectroscopy. Thus, CD was employed and the PES experiments were carried out before and after the CD treatments.

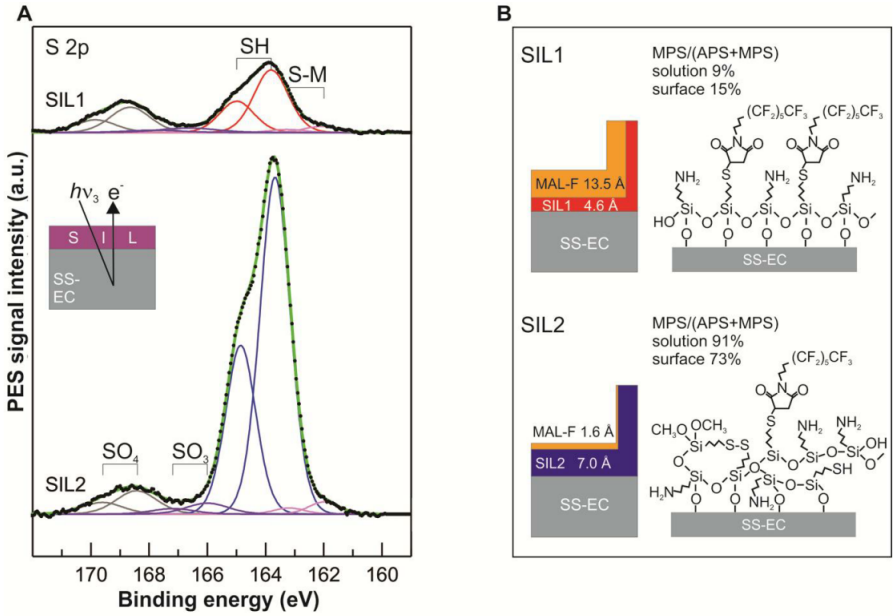

Figure 4.9. SR-PES results showing S 2p spectra and IEEB analysis after chemical derivatization (CD). (A) S 2p spectra from samples SIL1 (top) and SIL2 (bottom) with fits indicating the presence of SH, S-Metal (S-M) and S–S bonds as well as SO_x and SO_4. Schematic inset demonstrates the information depth in SR-PES experiments with photon energy $h\nu_3$ of 300 eV. (B) Results from IEEB analysis shown as schematic drawings for SIL1 and SIL2 before (red and blue, corresponding to spectra in A) and after (orange) CD. MPS/APS ratios on the surface are determined from the SR-PE spectra measured with photon energy of 550 eV. Schematic illustrations on the right show the proposed monolayer configuration of SIL1 (top) and clustered thicker overlayer of SIL2 (bottom). For clarity, some Si-O-bonds are omitted from the figure. [Paper IV]

Figure 4.9 shows that after TCEP and MAL-F treatments, more MAL-F is covalently adsorbed on APS 0.1/MPS0.01 than on APS 0.10/MPS1.00 even with almost 4 times higher SH concentration on APS 0.10/MPS1.00. This indicates that as the amount of surface MPS increases, the surface orientation of the silanes becomes more random than on small MPS surface concentration. Similar observations were made when the role of TCEP was investigated on APS/MPS and MPS samples.

Table 4.2. The relative surface concentration of fluorine after chemical derivatization.

sample	**F (at-%) after TCEP + MAL-F**	**F (at-%) after MAL-F**
MPS 0.10	13.7	0
APS 0.10/MPS0.01	3.8	5.3
APS 0.10/MPS0.10	10.2	1.3
APS 0.10/MPS1.00	2.2	0.9

Table 4.2 summarizes the relative surface concentration of fluorine, both after the sample exposure to TCEP and MAL-F and only to MAL-F. TCEP is used to estimate the MPS density at the surface. On MPS 0.10, no MAL-F is adsorbed without TCEP. Thus, most of the MPS at the surface is in a non-functional state, most likely in the form of MPS dimers with disulphide bonds (Figure 2.4). After TCEP treatment the relative surface concentration of MAL-F is high. On TCEP treated APS/MPS samples, on the other hand, the amount of surface MAL-F initially increases as the solution concentration of MPS increases. This indicates that on APS 0.10/MPS 0.01 and APS 0.10/MPS0.10 samples, the SH-groups are oriented upright. The drastic decrease in the MAL-F concentration on TCEP treated APS 0.10/MPS 1.00 samples is due to clustering promoted by partly hydrolyzed MPS. The lack of silane OH groups prevents optimal orientation of MPS and the SH groups are not available for MAL-F binding in the same extend than on highly ordered samples.

The difference in MAL-F binding with and without TCEP can be used to estimate the amount of disulphide bonds and, thus, the spatial distribution of MPS in the APS matrix. At low MPS surface concentration (APS 0.10/MPS0.01), the MPS are distributed so far from each other that annealing does not lead to significant amount of disulphide bonds. In fact, the unexpected higher MAL-F surface concentration on only MAL-F treated APS 0.10/MPS0.01 sample compared with TCEP and MAL-F treated is due to small variations in the thiol concentration of silanized samples (see Figure 4.7 (c)).With APS 0.10/MPS0.10, the surface concentration of MPS is ca. 40% higher than on APS 0.10/MPS0.01 and thus, larger amount of MPS are adjoining which leads to higher amount of disulphide bonds and significant difference in the MAL-F binding with the TCEP treated sample. As the MPS are oriented outwards, the SH groups are available for binding with MAL-F. With high MPS surface concentrations the TCEP treatment does not significantly increase the MAL-F binding as the SH or S-S groups are not spatially available for large MAL-F molecules.

Biofunctionality of the APS 0.10/MPS 0.01 surface was studied by coupling maleimide and biotin terminated PEG molecules (MAL-PEG-Biotin) to the MPS and PEG succinimidyl ester (NHS-PEG) to APS. The presence and orientation of biotin on the surface was detected with streptavidin-alkaline phosphatase protein complexes. Streptavidin has a high affinity to biotin. The presence of streptavidin-alkaline phosphatase at the surface can be detected by p-nitrophenyl phosphate. The yellow reaction product (p-nitrophenol) is catalysed by alkaline phosphatase. The relative amount of active biotin (covalently coupled to the silane layer and

available for biotin-avidin interaction) is detected by absorbance at 405 nm. The results show that stainless steel surfaces can be biotinylated via bifunctional APS/MPS monolayer although the surface is not yet adequately resistant to non-specific binding of proteins. This is significant for two reasons. Firstly, there are an enormous number of both biotin and (strept)avidin functionalized molecules commercially available. Hence, the biotinylated silane overlayer could be used for a plethora of biofunctional applications, where stainless steel is a valid substrate. Secondly, the ability of MPS to bind both MAL-F and MAL-PEG-Biotin shows that the APS/MPS on steel is a promising model for bifunctionalization of any metal or metal alloy surfaces. [Paper IV]

5. SUMMARY AND OUTLOOK

In this thesis, the adsorption and self-assembly phenomena of small organic molecules on metal and metal alloy surfaces have been studied mainly with photoelectron spectroscopy. Figure 5.1 summarizes the surface phenomena and studied organic-inorganic interfaces.

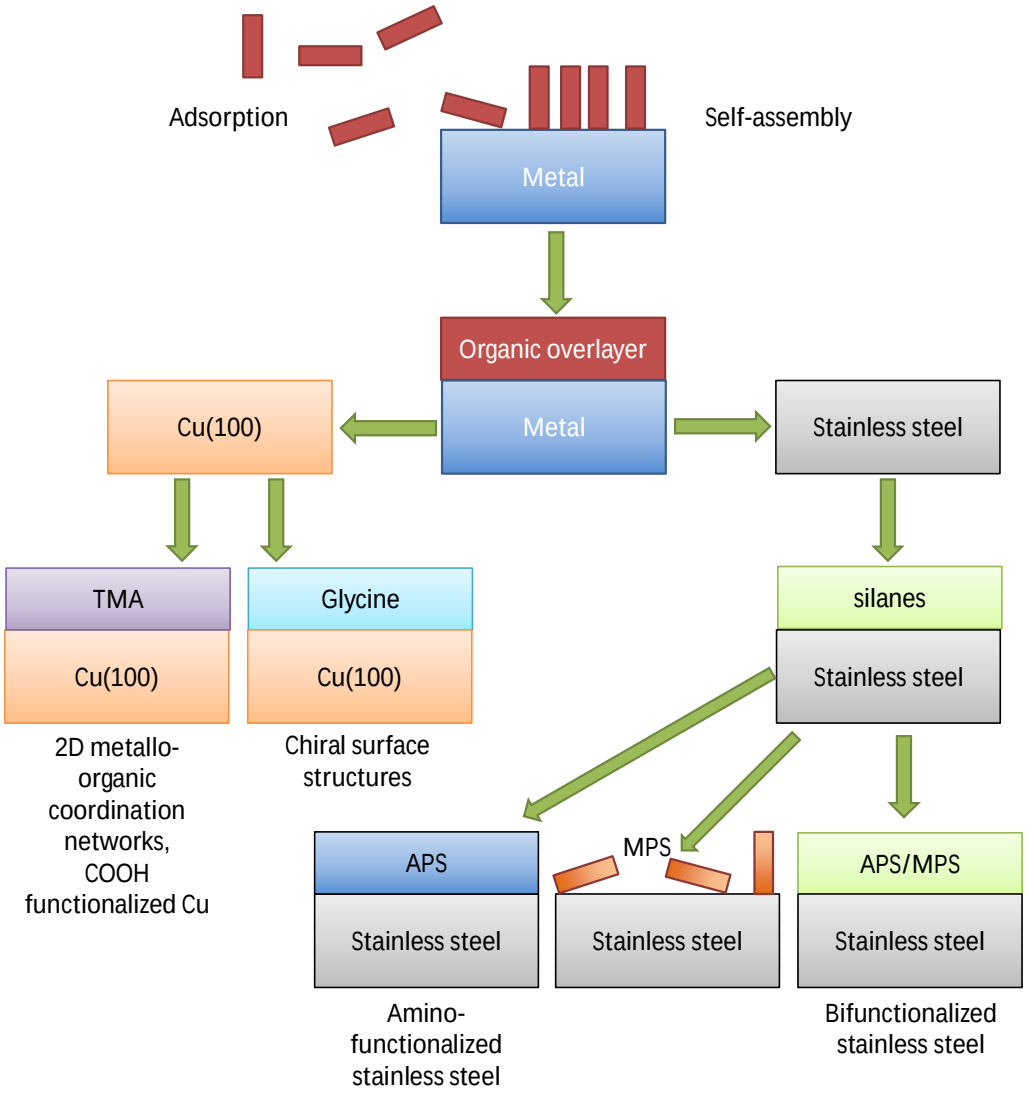

Figure 5.1. Summary of the organic-inorganic interfaces studied in this thesis.

Although the adsorption configurations on all studied systems are driven by self-assembly, the fabrication parameters must be controlled in order to obtain highly ordered, functional organic overlayers at a nanometre scale. The adsorption and molecular orientation of TMA on Cu(100) is mostly governed by TMA coverage, whereas glycine adsorption on the same substrate does not exhibit strong coverage dependent changes in the surface bonding of glycine. By employing the same deposition parameters for APS and MPS, a densely packed

APS monolayer on stainless steel is formed, but MPS only randomly adsorbed with significantly less than monolayer coverage. When both APS and MPS are coadsorbed, well-ordered, bifunctional monolayers are created, when the solution concentration of MPS is relatively small. Increasing amount of MPS, though, increases the non-uniform molecular orientation of both MPS and APS.

Photoelectron spectroscopy was the main experimental analysis method of the thesis complemented with scanning tunnelling microscopy for TMA and glycine on Cu(100). In addition to the elemental and chemical analysis of the surface, inelastic electron energy-loss background analysis was performed in order to gain information on the surface morphology of TMA/Cu(100) and silane on stainless steel samples. Spectromicroscopy gained important information on the origin of thick (>200 Å) clusters on silane surfaces. Synchrotron radiation mediated photoelectron spectroscopy enabled the non-destructive depth profiling of the studied samples. This was especially beneficial for the study of silanes on steel, because the elements in silanes are also present in the stainless steel substrate. The functionality of the APS/MPS overlayer i.e. the availability for the MPS in the APS matrix to bind maleimide functionalized molecules was studied with chemical derivatization photoelectron spectroscopy and by biofunctionalizing the surface with biotinylated maleimide.

The information gained on the studies of silanization of stainless steel is valuable, since the biofunctional stainless steel surfaces have a wide range of potential applications such as antifouling or antibacterial, implant or sensor surfaces. The gained knowledge on silanization can be transferred to other silanes and substrates and for different applications. The bifunctionalization concept could provide commercially interesting solutions in addition to biofunctional surfaces in adhesive, corrosion preventive, omniphobic and various other applications.

For the successful functionalization of inorganic substrates with organofunctional silanes, the properties of the substrate and the silanes must be studied with emphasis on the substrate hydroxylation and the control over the hydrolysis and condensation rates in the liquid phase. The SR-PES is crucially important analysis method for these types of surfaces. In the future, more knowledge would be gained, if the PES experiments would be complimented with atomic force microscopy and surface sensitive infrared spectroscopy methods. For biofunctional “sandwhich” structures and for silanes as an adhesive layer in between

materials, high kinetic energy SR-PES studies would be valuable as they provide information of interfaces and materials buried deeper than the sampling depth of XPS. The determination of the hydrolysis and condensation rates of the silanes in the liquid phase under different conditions (concentration, pH, amount of water etc.) would be beneficial for the optimization of the liquid phase deposition.

For the future studies of bifunctional silane overlayers, different approaches to LPD are worth testing. Depending on the silane species, the silanes could be hydrolysed in different solutions and mixed together prior to the silanization. Other possibilities such as sequential or layered silanization, could be used to create different chemical functionalities at the surface. Although the research performed for this thesis indicates that the studied silane overlayers are relatively stable in atmospheric conditions for long periods of time, in the future emphasis must be put on the determination of the stability of the silane overlayers in different media such as air, humid conditions, water, solvents and physiological conditions.

The nanofabrication self-assembly driven functionalization of metal and metal alloy surfaces provides an enormous amount of possibilities to render the surface rich of new functional properties. The studies of organic molecule adsorption on single crystal surfaces in highly controlled UHV conditions provide profound information that helps to understand the behaviour of large complex biomolecules, such as proteins and DNA at surfaces. The 2D metallo-organic networks may have future applications for instance in molecular electronics and catalysis. On the other hand, silanization is widely studied and also widely industrially used method for coating metal and alloy surfaces. Still, research on the molecular orientation of silanes and hence the functionality of the silane overlayer and nanomolecular bi- or multifunctional silane systems are not extensively studied and deserve to be researched further.

REFERENCES

[1] S. M. Barlow and R. Raval, “Complex organic molecules at metal surfaces: bonding, organisation and chirality,” *Surface Science Reports*, vol. 50, no. 6–8, pp. 201–341, 2003.

[2] S. Pan, A. K. Kota, J. M. Mabry, and A. Tuteja, “Superomniphobic Surfaces for Effective Chemical Shielding,” *Journal of the American Chemical Society*, vol. 135, no. 2, pp. 578–581, 2013.

[3] J. Hong and F. Zaera, “Interference of the Surface of the Solid on the Performance of Tethered Molecular Catalysts,” *Journal of the American Chemical Society*, vol. 134, no. 31, pp. 13056–13065, 2012.

[4] D. D. Gandhi, M. Lane, Y. Zhou, A. P. Singh, S. Nayak, U. Tisch, M. Eizenberg, and G. Ramanath, “Annealing-induced interfacial toughening using a molecular nanolayer,” *Nature*, vol. 447, no. 7142, pp. 299–302, 2007.

[5] A. Arranz, C. Palacio, D. García-Fresnadillo, G. Orellana, A. Navarro, and E. Muñoz, “Influence of Surface Hydroxylation on 3-Aminopropyltriethoxysilane Growth Mode during Chemical Functionalization of GaN Surfaces: An Angle-Resolved X-ray Photoelectron Spectroscopy Study,” *Langmuir*, vol. 24, no. 16, pp. 8667–8671, 2008.

[6] C. Séguin, J. M. McLachlan, P. R. Norton, and F. Lagugné-Labarthet, “Surface modification of poly(dimethylsiloxane) for microfluidic assay applications,” *Applied Surface Science*, vol. 256, no. 8, pp. 2524–2531, 2010.

[7] L. Selegård, V. Khranovskyy, F. Söderlind, C. Vahlberg, M. Ahrén, P.-O. Käll, R. Yakimova, and K. Uvdal, “Biotinylation of ZnO Nanoparticles and Thin Films: A Two-Step Surface Functionalization Study,” *ACS Applied Materials & Interfaces*, vol. 2, no. 7, pp. 2128–2135, 2010.

[8] A. J. Paula, D. Stéfani, A. G. Souza Filho, Y. A. Kim, M. Endo, and O. L. Alves, “Surface Chemistry in the Process of Coating Mesoporous SiO2 onto Carbon Nanotubes Driven by the Formation of Si–O–C Bonds,” *Chemistry - A European Journal*, vol. 17, no. 11, pp. 3228–3237, 2011.

[9] P. J. O’Brien, S. Shenogin, J. Liu, P. K. Chow, D. Laurencin, P. H. Mutin, M. Yamaguchi, P. Keblinski, and G. Ramanath, “Bonding-induced thermal conductance enhancement at inorganic heterointerfaces using nanomolecular monolayers,” *Nature Materials*, vol. 12, no. 2, pp. 118–122, 2012.

[10] A. Najari, P. Lang, P. C. Lacaze, and D. Mauer, “A new organofunctional methoxysilane bilayer system for promoting adhesion of epoxidized rubber to zinc,” *Progress in Organic Coatings*, vol. 64, no. 4, pp. 392–404, 2009.

[11] J. Singh and J. E. Whitten, “Adsorption of 3-Mercaptopropyltrimethoxysilane on Silicon Oxide Surfaces and Adsorbate Interaction with Thermally Deposited Gold,” *The Journal of Physical Chemistry C*, vol. 112, no. 48, pp. 19088–19096, 2008.

[12] J. P. Matinlinna, J. K.-H. Tsoi, J. de Vries, and H. J. Busscher, “Characterization of novel silane coatings on titanium implant surfaces,” *Clinical Oral Implants Research*, vol. 24, no. 6, pp. 688–697, 2013.

[13] S. R. Meyers and M. W. Grinstaff, “Biocompatible and Bioactive Surface Modifications for Prolonged In Vivo Efficacy,” *Chemical Reviews*, vol. 112, no. 3, pp. 1615–1632, 2012.

[14] J. L. Zimmermann, T. Nicolaus, G. Neuert, and K. Blank, “Thiol-based, site-specific and covalent immobilization of biomolecules for single-molecule experiments,” *Nature Protocols*, vol. 5, no. 6, pp. 975–985, 2010.

[15] F. Buth, A. Donner, M. Sachsenhauser, M. Stutzmann, and J. A. Garrido, “Biofunctional Electrolyte-Gated Organic Field-Effect Transistors,” *Advanced Materials*, vol. 24, no. 33, pp. 4511–4517, 2012.

[16] B. Bhushan, K. J. Kwak, S. Gupta, and S. C. Lee, “Nanoscale adhesion, friction and wear studies of biomolecules on silane polymer-coated silica and alumina-based surfaces,” *Journal of The Royal Society Interface*, vol. 6, no. 37, pp. 719–733, 2009.

[17] A. Caro, V. Humblot, C. Méthivier, M. Minier, L. Barbes, J. Li, M. Salmain, and C.-M. Pradier, “Bioengineering of stainless steel surface by covalent immobilization of enzymes. Physical characterization and interfacial enzymatic activity,” *Journal of colloid and interface science*, vol. 349, no. 1, pp. 13–18, 2010.

[18] J. Schartner, J. Güldenhaupt, B. Mei, M. Rögner, M. Muhler, K. Gerwert, and C. Kötting, “Universal Method for Protein Immobilization on Chemically Functionalized Germanium Investigated by ATR-FTIR Difference Spectroscopy,” *Journal of the American Chemical Society*, vol. 135, no. 10, pp. 4079–4087, 2013.

[19] M. Minier, M. Salmain, N. Yacoubi, L. Barbes, C. Méthivier, S. Zanna, and C.-M. Pradier, “Covalent immobilization of lysozyme on stainless steel. Interface spectroscopic characterization and measurement of enzymatic activity,” *Langmuir*, vol. 21, no. 13, pp. 5957–5965, 2005.

[20] D. Kregiel, “Advances in biofilm control for food and beverage industry using organo-silane technology: A review,” *Food Control*, vol. 40, pp. 32–40, 2014.

[21] V. Humblot, F. Tielens, N. B. Luque, H. Hampartsoumian, C. Méthivier, and C.-M. Pradier, “Characterization of Two-Dimensional Chiral Self-Assemblies L - and D - Methionine on Au(111),” *Langmuir*, vol. 30, no. 1, pp. 203–212, 2014.

[22] B. Kasemo, “Biological surface science,” *Surface Science*, vol. 500, no. 1–3, pp. 656–677, 2002.

[23] S. Onclin, B. J. Ravoo, and D. N. Reinhoudt, “Engineering Silicon Oxide Surfaces Using Self-Assembled Monolayers,” *Angewandte Chemie International Edition*, vol. 44, no. 39, pp. 6282–6304, 2005.

[24] K. K. Johannes V. Barth, Giovanni Costantini, “Engineering atomic and molecular nanostructures at surfaces,” *Nature*, vol. 437, p. 671, 2005.

[25] C. M. Niemeyer, “Nanoparticles, Proteins, and Nucleic Acids: Biotechnology Meets Materials Science,” *Angewandte Chemie International Edition*, vol. 40, no. 22, pp. 4128–4158, 2001.

[26] N. Miyashita and D. G. Kurth, “Directing supramolecular assemblies on surfaces,” *Journal of Materials Chemistry*, vol. 18, pp. 2636–2649, 2008.

[27] G. M. Whitesides and M. Boncheva, “Beyond molecules: Self-assembly of mesoscopic and macroscopic components,” *Proceedings of the National Academy of Sciences*, vol. 99, no. 8, pp. 4769–4774, 2002.

[28] J. V. Barth, “Molecular Architectonic on Metal Surfaces,” *Annual Review of Physical Chemistry*, vol. 58, no. 1, pp. 375–407, 2007.

[29] G. A. Somorjai, *Introduction to Surface Chemisty and Catalysis*, 2nd ed. Hoboken, New Jersey, U.S.: John Wiley & Sons, 2010.

[30] K. Oura, V. G. Lifshits, A. A. Saranin, A. V. Zotov, and M. Katayama, *Surface Science: an introduction*, 1 st. Berlin Heidelberg, Germany: Springer-Verlag, 2003.

[31] T. Classen, M. Lingenfelder, Y. Wang, R. Chopra, C. Virojanadara, U. Starke, G. Costantini, G. Fratesi, S. Fabris, S. deGironcoli, S. Baroni, S. Haq, R. Raval, and K. Kern, “Hydrogen and Coordination Bonding Supramolecular Structures of Trimesic Acid on Cu(110),” *Journal of Physical Chemistry A*, vol. 111, no. 49, pp. 12589–12603, 2007.

[32] J. V. Barth, “Fresh perspectives for surface coordination chemistry,” *Surface Science*, vol. 603, no. 10–12, pp. 1533–1541, 2009.

[33] P. Messina, A. Dmitriev, N. Lin, H. Spillmann, M. Abel, J. V. Barth, and K. Kern, “Direct Observation of Chiral Metal-Organic Complexes Assembled on a Cu(100) Surface,” *Journal of the American Chemical Society*, vol. 124, no. 47, pp. 14000–14001, 2002.

[34] H. Spillmann, A. Dmitriev, N. Lin, P. Messina, J. V. Barth, and K. Kern, “Hierarchical Assembly of Two-Dimensional Homochiral Nanocavity Arrays,” *Journal of the American Chemical Society*, vol. 125, no. 35, pp. 10725–10728, 2003.

[35] S. Stepanow, N. Lin, J. V. Barth, and K. Kern, “Non-covalent binding of fullerenes and biomolecules at surface-supported metallosupramolecular receptors,” *Chemical Communications*, no. 20, pp. 2153–2155, 2006.

[36] S. L. Tait, Y. Wang, G. Costantini, N. Lin, A. Baraldi, F. Esch, L. Petaccia, S. Lizzit, and K. Kern, “Metal−Organic Coordination Interactions in Fe−Terephthalic Acid Networks on Cu(100),” *Journal of the American Chemical Society*, vol. 130, no. 6, pp. 2108–2113, 2008.

[37] K. Kanazawa, A. Taninaka, O. Takeuchi, and H. Shigekawa, “What Orchestrates the Self-Assembly of Glycine Molecules on Cu(100)?,” *Physical Review Letters*, vol. 99, no. 21, 2007.

[38] Z.-X. Hu, W. Ji, and H. Guo, “Molecular ordering of glycine on Cu(100): The p(2×4) superstructure,” *Physical Review B*, vol. 84, no. 8, 2011.

[39] J.-H. Kang, R. L. Toomes, M. Polcik, M. Kittel, J.-T. Hoeft, V. Efstathiou, D. P. Woodruff, and A. M. Bradshaw, “Structural investigation of glycine on Cu(100) and comparison to glycine on Cu(110),” *The Journal of Chemical Physics*, vol. 118, no. 13, p. 6059, 2003.

[40] V. Efstathiou and D. P. Woodruff, “Characterisation of the interaction of glycine with Cu(1 0 0) and Cu(1 1 1),” *Surface Science*, vol. 531, no. 3, pp. 304–318, 2003.

[41] L. A. Nguyen, H. He, and C. Pham-Huy, “Chiral drugs: an overview,” *International Journal Biomedical Science*, vol. 2, no. 2, pp. 85–100, 2006.

[42] N. Graf, E. Yegen, T. Gross, A. Lippitz, W. Weigel, S. Krakert, A. Terfort, and W. E. S. Unger, “XPS and NEXAFS studies of aliphatic and aromatic amine species on functionalized surfaces,” *Surface Science*, vol. 603, no. 18, pp. 2849–2860, 2009.

[43] M. Arroyo-Hernández, J. Pérez-Rigueiro, and J. M. Martínez-Duart, “Formation of amine functionalized films by chemical vapour deposition,” *Materials Science and Engineering C*, vol. 26, no. 5–7, pp. 938–941, 2006.

[44] M. Arroyo-Hernández, J. Pérez-Rigueiro, A. Conde, A. Climent, R. Gago, M. Manso, and J. M. Martínez-Duart, “Characterization of biofunctional thin films deposited by activated vapor silanization,” *Journal of Materials Research*, vol. 23, no. 7, pp. 1931–1939, 2008.

[45] S.-R. Yang and B. O. Kolbesen, “A comparative study of the growth of octadecyltrichlorosilane and 3-mercaptopropyltrimethoxysilane self-assembled

monolayers on hydrophilic silicon surfaces," *Applied Surface Science*, vol. 255, no. 5 PART 1, pp. 1726–1735, 2008.

[46] E. Mäkilä, L. M. Bimbo, M. Kaasalainen, B. Herranz, A. J. Airaksinen, M. Heinonen, E. Kukk, J. Hirvonen, H. A. Santos, and J. Salonen, "Amine Modification of Thermally Carbonized Porous Silicon with Silane Coupling Chemistry," *Langmuir*, vol. 28, no. 39, pp. 14045–14054, 2012.

[47] B. Dorvel, B. Reddy, I. Block, P. Mathias, S. E. Clare, B. Cunningham, D. E. Bergstrom, and R. Bashir, "Vapor-Phase Deposition of Monofunctional Alkoxysilanes for Sub-Nanometer-Level Biointerfacing on Silicon Oxide Surfaces," *Advanced Functional Materials*, vol. 20, no. 1, pp. 87–95, 2010.

[48] C. Funk, P. M. Dietrich, T. Gross, H. Min, W. E. S. Unger, and W. Weigel, "Epoxy-functionalized surfaces for microarray applications: surface chemical analysis and fluorescence labeling of surface species: Epoxy-functionalized surfaces for microarray applications," *Surface and Interface Analysis*, vol. 44, no. 8, pp. 890–894, 2012.

[49] J. P. Matinlinna, A. H. Choi, and J. K.-H. Tsoi, "Bonding promotion of resin composite to silica-coated zirconia implant surface using a novel silane system," *Clinical Oral Implants Research*, vol. 24, no. 3, pp. 290–296, 2013.

[50] V. Sunkara and Y.-K. Cho, "Investigation on the mechanism of aminosilane-mediated bonding of thermoplastics and poly(dimethylsiloxane)," *ACS Applied Materials and Interfaces*, vol. 4, no. 12, pp. 6537–6544, 2012.

[51] R. Ngongang, E. Marceau, X. Carrier, C.-M. Pradier, C. Methivier, J.-L. Blanc, and M. Carre, "Surface passivation of aluminum alloy 6061 with gaseous trichlorosilane: A surface investigation," *Applied Surface Science*, vol. 292, pp. 165–173, 2014.

[52] H. J. Martin, K. H. Schulz, J. D. Bumgardner, and K. B. Walters, "XPS study on the use of 3-aminopropyltriethoxysilane to bond chitosan to a titanium surface," *Langmuir*, vol. 23, no. 12, pp. 6645–6651, 2007.

[53] N. Villard, C. Seneviratne, J. K. H. Tsoi, M. Heinonen, and J. Matinlinna, "Candida albicans aspects of novel silane system-coated titanium and zirconia implant surfaces," *Clinical Oral Implants Research*, vol. 00, pp. 1-10, 2014.

[54] T. D. Sargeant, M. S. Rao, C.-Y. Koh, and S. I. Stupp, "Covalent functionalization of NiTi surfaces with bioactive peptide amphiphile nanofibers," *Biomaterials*, vol. 29, no. 8, pp. 1085–1098, 2008.

[55] A. Najari, P. Lang, P. C. Lacaze, and D. Mauer, "Adsorption of γ-mercaptopropyltrimethoxysilane on zinc: A study of the competition between thiol and silanol functions related to the age of the siloxane solution, its pH and the oxidation state of the surface," *Surface Science*, vol. 606, no. 3–4, pp. 137–145, 2012.

[56] P. Jussila, H. Ali-Löytty, K. Lahtonen, M. Hirsimäki, and M. Valden, “Effect of surface hydroxyl concentration on the bonding andmorphology of aminopropylsilane thin films on austenitic stainless steel,” *Surface and Interface Analysis*, vol. 42, no. 3, pp. 157–164, 2010.

[57] J. M. Chovelon, L. E. Aarch, M. Charbonnier, and M. Romand, “Silanization of Stainless Steel Surfaces: Influence of Application Parameters,” *The Journal of Adhesion*, vol. 50, no. 1, pp. 43–58, 1995.

[58] F. Sinapi, A. Naji, J. Delhalle, and Z. Mekhalif, “Assessment by XPS and electrochemical techniques of two molecular organosilane films prepared on stainless-steel surfaces,” *Surface and Interface Analysis*, vol. 36, no. 11, pp. 1484–1490, 2004.

[59] C.-K. Kang and Y.-S. Lee, “The surface modification of stainless steel and the correlation between the surface properties and protein adsorption,” *Journal of Materials Science: Materials in Medicine*, vol. 18, no. 7, pp. 1389–1398, 2007.

[60] M. Honkanen, M. Hoikkanen, M. Vippola, J. Vuorinen, T. Lepistö, P. Jussila, H. Ali-Löytty, M. Lampimäki, and M. Valden, “Characterization of silane layers on modified stainless steel surfaces and related stainless steel-plastic hybrids,” *Applied Surface Science*, vol. 257, no. 22, pp. 9335–9346, 2011.

[61] A. M. Slaney, V. A. Wright, P. J. Meloncelli, K. D. Harris, L. J. West, T. L. Lowary, and J. M. Buriak, “Biocompatible Carbohydrate-Functionalized Stainless Steel Surfaces: A New Method For Passivating Biomedical Implants,” *ACS Applied Materials & Interfaces*, vol. 3, no. 5, pp. 1601–1612, 2011.

[62] W. Guo, J. Zhu, Z. Cheng, Z. Zhang, and X. Zhu, “Anticoagulant Surface of 316 L Stainless Steel Modified by Surface-Initiated Atom Transfer Radical Polymerization,” *ACS Applied Materials & Interfaces*, vol. 3, no. 5, pp. 1675–1680, 2011.

[63] V. H. V. Sarmento, M. G. Schiavetto, P. Hammer, A. V. Benedetti, C. S. Fugivara, P. H. Suegama, S. H. Pulcinelli, and C. V. Santilli, “Corrosion protection of stainless steel by polysiloxane hybrid coatings prepared using the sol–gel process,” *Surface and Coatings Technology*, vol. 204, no. 16–17, pp. 2689–2701, 2010.

[64] E. M. E. Kristensen, F. Nederberg, H. Rensmo, T. Bowden, J. Hilborn, and H. Siegbahn, “Photoelectron Spectroscopy Studies of the Functionalization of a Silicon Surface with a Phosphorylcholine-Terminated Polymer Grafted onto (3-Aminopropyl)trimethoxysilane,” *Langmuir*, vol. 22, no. 23, pp. 9651–9657, 2006.

[65] A. K. Chauhan, D. K. Aswal, S. P. Koiry, S. K. Gupta, J. V. Yakhmi, C. Sürgers, D. Guerin, S. Lenfant, and D. Vuillaume, “Self-assembly of the 3-amino-propyltrimethoxysilane multilayers on Si and hysteretic current–voltage characteristics,” *Applied Physics A*, vol. 90, no. 3, pp. 581–589, 2008.

[66] N. Graf, A. Lippitz, T. Gross, F. Pippig, A. Holländer, and W. E. S. Unger, “Determination of accessible amino groups on surfaces by chemical derivatization with 3,5-bis(trifluoromethyl)phenyl isothiocyanate and XPS/NEXAFS analysis,” *Analytical and Bioanalytical Chemistry*, vol. 396, no. 2, pp. 725–738, 2010.

[67] P. Pallavicini, G. Dacarro, M. Galli, and M. Patrini, “Spectroscopic evaluation of surface functionalization efficiency in the preparation of mercaptopropyltrimethoxysilane self-assembled monolayers on glass,” *Journal of colloid and interface science*, vol. 332, no. 2, pp. 432–438, 2009.

[68] E. Lecoq, D. Duday, S. Bulou, G. Frache, F. Hilt, R. Maurau, and P. Choquet, “Plasma Polymerization of APTES to Elaborate Nitrogen Containing Organosilicon Thin Films: Influence of Process Parameters and Discussion About the Growing Mechanisms,” *Plasma Processes and Polymers*, vol. 10, no. 3, pp. 250–261, 2013.

[69] J.-H. Liu, Z.-W. Zhan, M. Yu, and S.-M. Li, “Adsorption behavior of glycidoxypropyl-trimethoxy-silane on titanium alloy Ti-6.5Al-1Mo-1V-2Zr,” *Applied Surface Science*, vol. 264, pp. 507–515, 2013.

[70] A. N. Parikh, D. L. Allara, I. B. Azouz, and F. Rondelez, “An intrinsic relationship between molecular structure in self-assembled n-alkylsiloxane monolayers and deposition temperature,” *Journal of Physical Chemistry*, vol. 98, no. 31, pp. 7577–7590, 1994.

[71] K. Wen, R. Maoz, H. Cohen, J. Sagiv, A. Gibaud, A. Desert, and B. M. Ocko, “Postassembly Chemical Modification of a Highly Ordered Organosilane Multilayer: New Insights into the Structure, Bonding, and Dynamics of Self-Assembling Silane Monolayers,” *ACS Nano*, vol. 2, no. 3, pp. 579–599, 2008.

[72] M. Hannula, “Effect of Silanization Parameters on the Composition of the Biofunctional Mixed Silane Thin Film Synthesized on Electrochemically Passivated Austenitic Steel,” Master of Science Thesis, Tampere University of Technology.

[73] P. D. Pollheimer, M. Kastner, A. Ebner, D. Blaas, P. Hinterdorfer, H. J. Gruber, and S. Howorka, “Receptor Arrays for the Selective and Efficient Capturing of Viral Particles,” *Bioconjugate Chemistry*, vol. 20, no. 3, pp. 466–475, 2009.

[74] R. Bhure and A. Mahapatro, “Silicon Based Nanocoatings on Metal Alloys and Their Role in Surface Engineering,” *Silicon*, vol. 2, no. 3, pp. 117–151, 2010.

[75] A. Ulman, “Formation and Structure of Self-Assembled Monolayers,” *Chem. Rev.*, vol. 96, no. 4, pp. 1533–1554, 1996.

[76] C. Y. K. Lung, E. Kukk, T. Hägerth, and J. P. Matinlinna, “Surface modification of silica-coated zirconia by chemical treatments,” *Applied Surface Science*, vol. 257, no. 4, pp. 1228–1235, 2010.

[77] R. A. Shircliff, I. T. Martin, J. W. Pankow, J. Fennell, P. Stradins, M. L. Ghirardi, S. W. Cowley, and H. M. Branz, "High-Resolution X-ray Photoelectron Spectroscopy of Mixed Silane Monolayers for DNA Attachment," *ACS Applied Materials & Interfaces*, vol. 3, no. 9, pp. 3285–3292, Sep. 2011.

[78] "Outokumpu product informations EN 1.4372, AISI 201." Outokumpu Tornio Works, 2009.

[79] P. Van der Heide, *X-ray photoelectron spectroscopy: an introduction to principles and practices*. Hoboken, N.J: Wiley, 2012.

[80] J. F. Moulder and J. Chastain, *Handbook of x-ray photoelectron spectroscopy: a reference book of standard spectra for identification and interpretation of XPS data*. Eden Prairie, Minn.: Physical Electronics Division, Perkin-Elmer Corp., 1992.

[81] D. Briggs and J. T. Grant, Eds., *Surface analysis by Auger and x-ray photoelectron spectroscopy*. Chichester, West Sussex, U.K: IM Publications, 2003.

[82] J. C. Ratner and D. D. Castner, "Electron Spectroscopy for Chemical Analysis," in *Surface analysis: the principal techniques*, 2nd ed., J. C. Vickerman and I. S. Gilmore, Eds. Chichester, U.K: Wiley, 2009.

[83] M. P. Seah and W. A. Dench, "Quantitative electron spectroscopy of surfaces: A standard data base for electron inelastic mean free paths in solids," *Surface and Interface Analysis*, vol. 1, no. 1, pp. 2–11, 1979.

[84] S. Tanuma, C. J. Powell, and D. R. Penn, "Calculation of electron inelastic mean free paths (IMFPs) VII. Reliability of the TPP-2M IMFP predictive equation," *Surface and Interface Analysis*, vol. 35, no. 3, pp. 268–275, 2003.

[85] P.-L. Girard-Lauriault, T. Gross, A. Lippitz, and W. E. S. Unger, "Chemical and Elemental Depth Profiling of Very Thin Organic Layers by Constant Kinetic Energy XPS: A New Synchrotron XPS Analysis Strategy," *Analytical Chemistry*, vol. 84, no. 14, pp. 5984–5991, 2012.

[86] G. Margaritondo, "X-ray Photoelectron Spectroscopy and Imaging at Synchrotrons," in D. Briggs and J.T. Grant (Eds), *Surface Analysis by Auger and X-Ray Photoelectron Spectroscopy*, 2003, Chichester, West Sussex, U.K: IM Publications, pp. 733-748, 2003.

[87] N. Vinogradov, "Controlling Electronic and Geometrical Structure of Honeycomb-Lattice Materials Supported on Metal Substrates Graphene and Hexagonal Boron Nitride," Dissertations from the Faculty of Science and Technology 1019, Uppsala University, Sweden, 2013.

[88] K. Lahtonen, M. Lampimäki, P. Jussila, M. Hirsimäki, and M. Valden, "Instrumentation and analytical methods of an x-ray photoelectron spectroscopy-

scanning tunneling microscopy surface analysis system for studying nanostructured materials," *Review of Scientific Instruments*, vol. 77, no. 8, 2006.

[89] P. M. Dietrich, T. Horlacher, P.-L. Girard-Lauriault, T. Gross, A. Lippitz, H. Min, T. Wirth, R. Castelli, P. H. Seeberger, and W. E. S. Unger, "Adlayers of Dimannoside Thiols on Gold: Surface Chemical Analysis," *Langmuir*, vol. 27, no. 8, pp. 4808–4815, 2011.

[90] J. J. Senkevich, G.-R. Yang, and T.-M. Lu, "Thermal stability of mercaptan terminated self-assembled multilayer films on SiO2 surfaces," *Colloids and Surfaces A: Physicochemical and Engineering Aspects*, vol. 207, no. 1–3, pp. 139–145, 2002.

[91] N. Fairley, *CasaXPS: Spectrum Processing Software for XPS, AES and SIMS (Version 2.3.16). Casa Software Ltd. Cheshire SK9 6N, www.casaxps.com UK, 2009.*

[92] M. Zharnikov, "High-resolution X-ray photoelectron spectroscopy in studies of self-assembled organic monolayers," *Journal of Electron Spectroscopy and Related Phenomena*, vol. 178–179, pp. 380–393, 2010.

[93] A. Dmitriev, N. Lin, J. Weckesser, J. V. Barth, and K. Kern, "Supramolecular Assemblies of Trimesic Acid on a Cu(100) Surface," *The Journal of Physical Chemistry B*, vol. 106, no. 27, pp. 6907–6912, 2002.

[94] S. Tougaard, "Quantification of Nanostructures by Electron Spectroscopy," in D. Briggs and J.T. Grant (Eds), *Surface Analysis by Auger and X-Ray Photoelectron Spectroscopy*, 2003, Chichester, West Sussex, U.K: IM Publications, pp. 295-344, 2003.

[95] S. Tougaard, "Energy loss in XPS: Fundamental processes and applications for quantification, non-destructive depth profiling and 3D imaging," *Journal of Electron Spectroscopy and Related Phenomena*, vol. 178–179, no. C, pp. 128–153, 2010.

[96] S. Tougaard, "Accuracy of the non-destructive surface nanostructure quantification technique based on analysis of the XPS or AES peak shape," *Surface and Interface Analysis*, vol. 26, no. 4, pp. 249–269, 1998.

[97] S. Tougaard, *QUASES: Software for Quantitative XPS/AES of Surface Nanostructures by Analysis of the Peak Shape and Background (Version 5.0)*, www.quases.com, 2003.

[98] H. Ali-Löytty, P. Jussila, and M. Valden, "Optimization of the electrical properties of Ti-Nb stabilized ferritic stainless steel SOFC interconnect alloy upon high-temperature oxidation: The role of excess Nb on the interfacial oxidation at the oxide-metal interface," *International Journal of Hydrogen Energy*, vol. 38, no. 2, pp. 1039–1051, 2013.

[99] H. Ali-Löytty, P. Jussila, T. Juuti, L. P. Karjalainen, A. A. Zakharov, and M. Valden, "Influence of precipitation on initial high-temperature oxidation of Ti-Nb stabilized

ferritic stainless steel SOFC interconnect alloy," *International Journal of Hydrogen Energy*, vol. 37, no. 19, pp. 14528–14535, 2012.

[100] H. Ali-Löytty, P. Jussila, M. Hirsimäki, and M. Valden, "Influence of CrN surface compound on the initial stages of high temperature oxidation of ferritic stainless steel," *Applied Surface Science*, vol. 257, no. 17, pp. 7783–7791, 2011.

[101] P. Jussila, H. Ali-Löytty, K. Lahtonen, M. Hirsimäki, and M. Valden, "Inhibition of initial surface oxidation by strongly bound hydroxyl species and Cr segregation: H2O and O2 adsorption on Fe-17Cr," *Surface Science*, vol. 603, no. 19, pp. 3005–3010, 2009.

[102] B. Mrabet, A. Mejbri, S. Mahouche, S. Gam-Derouich, M. Turmine, M. Mechouet, P. Lang, H. Bakala, M. Ladjimi, A. Bakhrouf, S. Tougaard, and M. M. Chehimi, "Controlled adhesion of Salmonella Typhimurium to poly(oligoethylene glycol methacrylate) grafts," *Surface and Interface Analysis*, vol. 43, no. 11, pp. 1436–1443, Nov. 2011.

[103] S. Gam-Derouich, B. Carbonnier, M. Turmine, P. Lang, M. Jouini, D. Ben Hassen-Chehimi, and M. M. Chehimi, "Electrografted Aryl Diazonium Initiators for Surface-Confined Photopolymerization: A New Approach to Designing Functional Polymer Coatings," *Langmuir*, vol. 26, no. 14, pp. 11830–11840, Jul. 2010.

[104] A. Khlifi, S. Gam-Derouich, M. Jouini, R. Kalfat, and M. M. Chehimi, "Melamine-imprinted polymer grafts through surface photopolymerization initiated by aryl layers from diazonium salts," *Food Control*, vol. 31, no. 2, pp. 379–386, Jun. 2013.

[105] E. Jagst, *Surface functional group characterization using chemical derivatization X-ray photoelectron spectroscopy (CD-XPS)*. Berlin: Bundesanstalt für Materialforschung und -prüfung (BAM), 2011.

[106] K. W. Kolasinski, *Surface Science Foundations and Catalysis and Nanoscience*, 2nd edition. Chisester, West Sussex, England: John Wiley Sons Ltd, 2008.

[107] M. Orio, D. A. Pantazis, and F. Neese, "Density functional theory," *Photosynthesis Research*, vol. 102, no. 2–3, pp. 443–453, Dec. 2009.

[108] A.-S. Duwez, "Exploiting electron spectroscopies to probe the structure and organization of self-assembled monolayers: a review," *Journal of Electron Spectroscopy and Related Phenomena*, vol. 134, no. 2–3, pp. 97–138, Feb. 2004.

[109] M. Wühn, J. Weckesser, and C. Wöll, "Bonding and Orientational Ordering of Long-Chain Carboxylic Acids on Cu(111): Investigations Using X-ray Absorption Spectroscopy," *Langmuir*, vol. 17, no. 24, pp. 7605–7612, Nov. 2001.

[110] F. Bournel, C. Laffon, P. Parent, and G. Tourillon, “Adsorption of some substituted ethylene molecules on Pt(111) at 95 K Part 1: NEXAFS, XPS and UPS studies,” *Surface Science*, vol. 350, no. 1–3, pp. 60–78, Apr. 1996.

[111] N. Lin, A. Dmitriev, J. Weckesser, J. V. Barth, and K. Kern, “Real-Time Single-Molecule Imaging of the Formation and Dynamics of Coordination Compounds,” *Angewandte Chemie International Edition*, vol. 41, no. 24, pp. 4779–4783, Dec. 2002.

[112] N. Lin, D. Payer, A. Dmitriev, T. Strunskus, C. Wöll, J. V. Barth, and K. Kern, “Two-Dimensional Adatom Gas Bestowing Dynamic Heterogeneity on Surfaces,” *Angewandte Chemie International Edition*, vol. 44, no. 10, pp. 1488–1491, Feb. 2005.

[113] K. Kanazawa, Y. Sainoo, Y. Konishi, S. Yoshida, A. Taninaka, A. Okada, M. Berthe, N. Kobayashi, O. Takeuchi, and H. Shigekawa, “Anisotropic Free-Electron-Like Dispersions and Standing Waves Realized in Self-Assembled Monolayers of Glycine on Cu(100),” *Journal of the American Chemical Society*, vol. 129, no. 4, pp. 740–741, Jan. 2007.

[114] X. Zhao, H. Wang, R. G. Zhao, and W. S. Yang, “Self-assembly of amino acids on the Cu(001) surface,” *Materials Science and Engineering: C*, vol. 16, no. 1–2, pp. 41–50, Oct. 2001.

Tampereen teknillinen yliopisto
PL 527
33101 Tampere

Tampere University of Technology
P.O.B. 527
FI-33101 Tampere, Finland

ISBN 978-952-15-3410-2
ISSN 1459-2045